

Anisotropic fracture behavior of the 3rd generation advanced high-strength – Quenching and Partitioning steels: Experiments and simulation

Zinan Li^a, Fuhui Shen^{a,b,*}, Yi Liu^c, Christoph Hartmann^d, Roman Norz^d, Sebastian Müntermann^b, Wolfram Volk^d, Junying Min^c and Junhe Lian^{a,**}

^a Advanced Materials and Manufacturing, Department of Mechanical Engineering,
Aalto University, 02150 Espoo, Finland

^b Institute of Metal Forming, RWTH Aachen University, Intzestraße 1, 52072 Aachen,
Germany

^c School of Mechanical Engineering, Tongji University, Shanghai 201804, China

^d Chair of Metal Forming and Casting, Technical University of Munich, Garching
85748, Germany

*Fuhui.shen@aalto.fi; Fuhui.shen@ibf.rwth-aachen.de

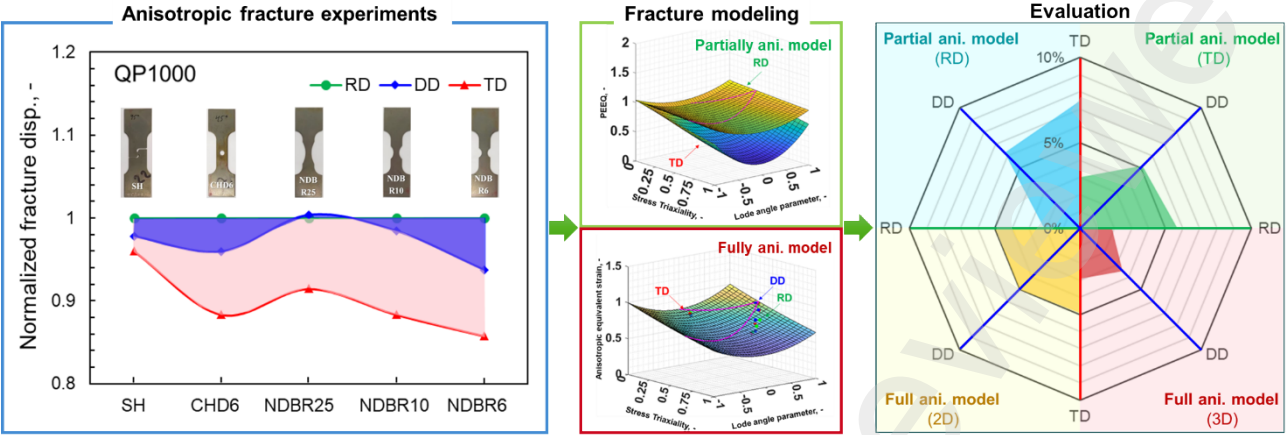
**Phone: +358 50 477 0765

junhe.lian@aalto.fi

Highlights:

- Pronounced anisotropic fracture exists in a high-strength QP1000 steel.
- Anisotropic fracture shows dependency on stress states.
- Higher stress triaxiality intensifies the anisotropic fracture.
- Partially anisotropic fracture models cannot accurately predict fracture along different directions.
- A fully anisotropic fracture model is formulated and provides precise prediction.

Graphic abstract:



Abstract:

Advanced high-strength steels (AHSS) have revolutionized the automotive industry by reducing weight without compromising crashworthiness. The new third-generation steels, such as quenching and partitioning (QP) steels, offer exceptional strength and ductility. However, despite the extensive strength-ductility studies, there is a wide knowledge gap in the literature on the fracture behavior of QP steels under a large range of stress states and loading conditions for material forming operations. This study aims to systematically investigate the fracture behavior of QP1000 sheet metal through a combination of experimental and numerical approaches. In addition to the classic fracture dependency on stress states, we particularly focus on the anisotropic behavior in terms of both plasticity and fracture. Mechanical tests with digital image correlation are performed along three loading directions covering stress states from simple shear to plane-strain tension. The evolving non-associated Hill48 (enHill48) model is employed to describe anisotropic plasticity, while the fracture behavior is represented by a partially anisotropic fracture model and a fully anisotropic fracture model. It is concluded that the investigated QP steel shows noticeable yet minor anisotropic plasticity behavior but owns strong fracture dependency on anisotropy and the dependency intensifies with the increase of stress triaxiality. The partially anisotropic fracture model, which has shown success for materials with minor anisotropic plasticity, fails to describe the anisotropic fracture and a fully anisotropic model provides excellent predictive capability.

Keywords: Quenching and partitioning steel; Anisotropy; Ductile fracture; Evolving plasticity; Anisotropic fracture; Constitutive model.

1 Introduction

Advanced high-strength steels (AHSS) have been developed in the automotive industries to effectively improve fuel economy by reducing the weight without compromising the crashworthiness of the structure [1]. The strength level of the first-generation (1st G) AHSS has been elevated beyond 800 MPa from traditional high-strength steels. However, excellent strength usually comes with the sacrifice of ductility. Such a dilemma has been solved with the significantly promoted third-generation (3rd G) steels [2]. One typical example is the quenching and partitioning (QP) steels, offering a superior combination of strength and ductility due to their high amount of tempered martensite and the phase transformation-induced plasticity [3-10].

Among the widely adopted grades, QP1000 has attracted the most attention due to its high relevance in automotive applications [11]. With similar strength to dual-phase or complex-phase steels currently used in the market but more than doubled elongation (25%-30%), it shows an obvious advantage in cold forming processes and crashworthiness properties. However, tensile properties cannot represent the complete required performance in terms of manufacturing particularly when it involves local deformation, e.g., shearing, bending, edge forming, etc. Therefore, numerous experimental tests have been developed and conducted in the past decades to characterize the local fracture behavior of AHSS, e.g., bendability [12], edge formability [13], and general ductile fracture [14] under various stress states. However, for the 3rd G steels, especially for QP steels, while a large amount of research effort has been evident in the design of the heat treatment processes [15] and understanding of the correlation between microstructure and tensile properties [16], the studies focusing on the local fracture behavior are extremely limited, which hinders accelerating the use of these high-performance steels in industry. Therefore, a thorough characterization of the fracture behavior of this steel grade under a wide range of stress states that represent all possible forming scenarios for sheet metals is urgently needed.

Based on extensive studies focusing on this topic of the 1st G AHSS and many other engineering alloys, the fracture behavior of these high-strength steels shows distinct and diverse dependency on the stress states, characterized by stress triaxiality and Lode angle [12, 17-23]. Correspondingly, the coupled (the damage-induced softening is considered in the flow behavior), e.g., the Gurson-type models [24-33], uncoupled (damage is not coupled with flow behavior), e.g., the Modified Mohr-Coulomb (MMC) model [21], and the Hosford-Coulomb model [19] and hybrid (switchable between coupled and uncoupled) models, e.g., the hybrid damage mechanics (HDM) model [34], have been developed to account for the dependency of ductile fracture on stress states [35]. For a more comprehensive review of the model development, readers are referred to Pineau et al. [36] oriented on more materials side, and Tekkaya et al. [37] for material forming related applications. In the context of the 3rd Gen steels, only recently, Wang et al. [38] made one of the first attempts to investigate the ductile fracture behavior of a QP980 steel sheet in a wide range of stress states. In the study, several phenomenological uncoupled models, including the Brozzo criterion [39], the Oh criterion [40], the Rice-Tracey criterion [41], and the DF2012 [42] were calibrated and used to describe the fracture behavior of QP980. However, material forming involves many more factors than stress states, such as temperature, strain rates, and loading paths. Among them, anisotropy has been identified as a critical one, anisotropic fracture has been pointed out by as a dominant factor in deciding edge formability under uniform out-of-plane loading, such as hole expansion and flanging [35].

While the anisotropic fracture behavior of QP steels remains blank in the current literature, several recent studies showed that this grade of steel possesses significant plasticity anisotropy. Chen et al. [43] showed that QP980 possessed pronounced plastic anisotropy and anisotropic hardening and proposed an analytical yield function under the non-associated flow rule to capture the anisotropic hardening behavior. Hou et al. [44] further discovered that QP980 and later QP1180 [45] also show adequate tension-compression asymmetry due to the stress-state-

dependent austenite-to-martensite phase transformation [46]. The same observation was confirmed by Zhang and Lou [47]. Under non-proportional loading conditions, Hou et al. [48] further showed that QP steels also demonstrate pronounced strain-dependent Bauschinger effect and permanent softening. With these very recent findings of QP steels demonstrating strong deformation-relevant anisotropy, it is urgently needed to investigate the anisotropic fracture behavior of the QP steels in a wide range of stress states that various sheet forming processes encounter.

This study, therefore, aims to investigate the anisotropic fracture behavior of a QP1000 sheet metal covering the stress states from simple shear, uniaxial tension, to plane strain tension via experiments conducted along the rolling, transverse, and diagonal directions. A hybrid experimental and numerical procedure will be employed to quantify the anisotropic fracture behavior. The anisotropic hardening and evolution of the plastic potential will be described by the evolving non-associated Hill 48 (enHill48) model [49]. The anisotropic fracture behavior will be modeled by the partially anisotropic fracture model as well as a full anisotropic fracture model based on linear tensor transformation. The performance of both formulations will be comprehensively analyzed and compared. Guidance will be provided based on the quantitative data to be employed for the prediction of the anisotropic fracture behavior of QP steels in terms of both accuracy and effort in calibration procedures.

2 Material and experiments

2.1 Material and experimental program

An as-received high-strength QP1000 steel with a measured thickness of about 1.4 mm was studied in this work. The chemical composition of the material is summarized in Table 1.

Table 1: Chemical composition of QP1000 (mass content in %).

C	Si	Mn	Al	P	S	Ti + Nb
0.15	1.67	2.42	0.074	<0.002	<0.002	0.011

The mechanical testing program is designed to comprehensively investigate the anisotropic effects on plasticity and ductile fracture, using optimized specimen geometries to cover the stress states relevant to sheet metal forming, as shown in Figure 1. The anisotropic plastic flow properties were experimentally characterized by performing uniaxial tensile tests at room temperature (RT, 25°C) under a quasi-static (QS, 0.0002 s⁻¹) strain rate, using smooth dog-bone (SDB) specimens cut along the rolling direction (RD), diagonal direction (DD), and transverse direction (TD). The equal-biaxial flow behavior was characterized by cruciform tests [44] at a small strain level (true strain < 0.1), and hydraulic bulge tests at large strains. The 230 mm × 230 mm bulge specimens were clamped by a blank holder with a diameter of 105 mm together with a 123 mm-diameter die and punched under the velocity of 3 mm/min with a clamping force of 600 kN.

The anisotropic fracture properties, from shear to plane strain tension, were investigated by applying remote uniaxial tension along RD, DD and TD to five types of specimens with featured shapes, including one shear (SH) specimen in optimized shape, one central-hole (CH) with a diameter of 6 mm (CHD6), and three notched dog-bone (NDB) specimens with radii of 25 mm (NDBR25), 10 mm (NDBR10) and 6 mm (NDBR6). The overall QS condition in the local deformation region was achieved by applying a crosshead velocity of 0.18 mm/min in all fracture tests. Three parallel tests were conducted for each geometry. A stereo digital image correlation (DIC) system was applied to measure the strain fields using two cameras, with a detecting resolution of 50 pixels/mm and an acquisition interval of 0.5 s. The surface of the specimen was lacquered with an even layer of white paint and then sprayed to form speckle patterns with a speckle diameter of 5-10 pixels. A parallel filter was placed in front of the spotlight to minimize the reflections from the material surface and achieve optimal lighting conditions.

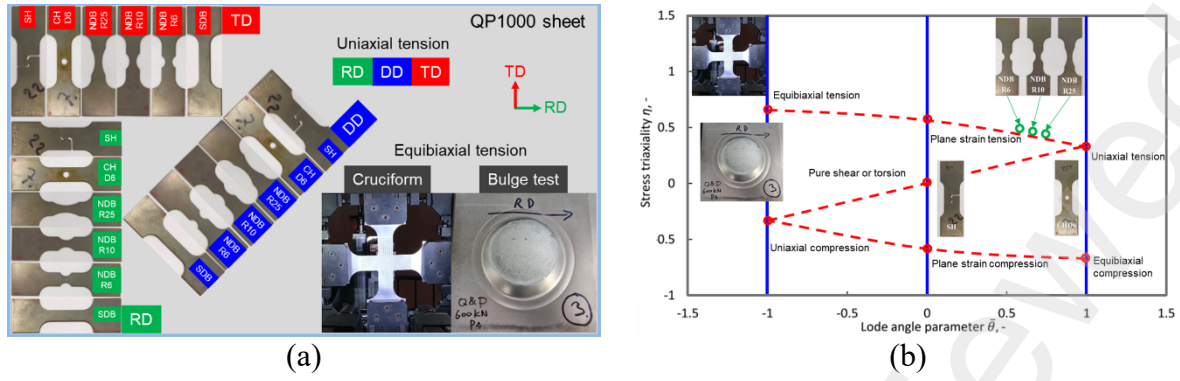


Figure 1: Overview of the experimental program on (a) material characterization tests, and (b) the range of stress triaxiality and Lode angle parameters covered from the tests.

2.2 Experimental results

The engineering and true stress–strain curves along RD, DD, and TD from uniaxial tensile tests are shown in Figure 2 (a) and (b), respectively. A very good repeatability is obtained from the parallel tests. The anisotropic uniaxial tensile properties, including yield strength (YS), ultimate tensile strength (UTS), uniform elongation (UE), and total elongation (TE), are shown in Figure 2 (c). The results reveal that QP1000 owns existing anisotropy in the strength values, while the ductility and fracture properties show moderate dependence on the loading direction. The characterized biaxial flow curve of the material obtained from the bulge test is shown in Figure 2 (b), which is used for calibrating the parameters in constitutive models. Lankford coefficients (r-values) in all three loading directions are smaller than one and keep evolving during deformation, as shown in Figure 2 (d). The detailed uniaxial tensile properties of three directions after averaging over repeating tests are summarized in Table 2.

For the fracture anisotropy, the logarithm axial strain contours of all specimens were obtained with stereo-DIC. As demonstrated with CHD6 (the last frame right before fracture) in Figure 3, the fracture strain values show a clear dependence on the loading direction, which is the highest along DD and the lowest along TD. The characteristic force and displacement (corresponding to a gauge length of 30 mm) curves are plotted in Figure 4 (a) to (d), where the last point is identified as the fracture moment. The anisotropic fracture behavior is significant

in the current material, as fracture force and displacement vary with the loading directions. The force and displacement curves of RD and DD almost overlap until the fracture point, while there is a noticeable difference in the values of fracture displacement and force. A general trend noticed for all geometries is that the specimens loaded along RD have the lowest fracture force and the longest fracture displacement. In contrast, the specimens loaded along TD have the highest fracture force and the shortest fracture displacement. It is observed that the variation in fracture displacement and force with loading direction is also affected by the stress states, i.e., specimen geometries. As shown in Figure 4 (e) to (f), the normalized fracture displacement and force (where results of RD are taken as reference) show dependency on the stress states. In particular, the anisotropic effects on the fracture force and displacement values are intensified with increasing stress triaxiality from SH to NDBR6.

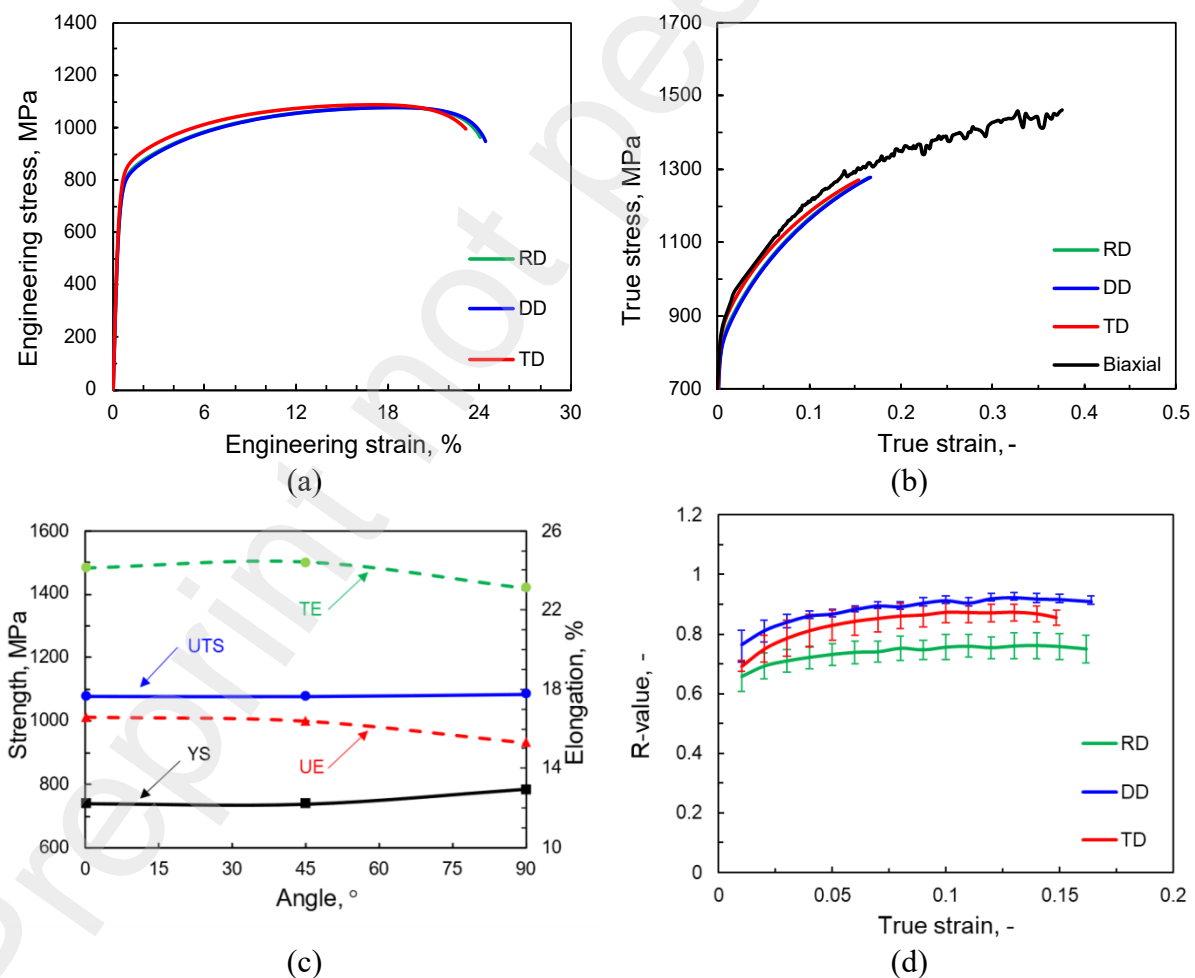


Figure 2: The characteristic tensile properties of QP1000 along three loading directions, (a) engineering stress–strain curves of uniaxial tension, (b) true stress–strain curves of uniaxial and

biaxial tension (c) distribution of tensile properties, and (d) averaged r-value curves of uniaxial tension with scatters.

Table 2: Summary of uniaxial tensile properties at room temperature for QP1000.

Directions \ Properties	YS, MPa	UTS, MPa	UE, %	TE, %	r-value at UE, -
RD	739.6	1077.4	16.6	24.1	0.75
DD	738.0	1076.7	16.4	24.4	0.91
TD	783.1	1085.3	15.3	23.1	0.86

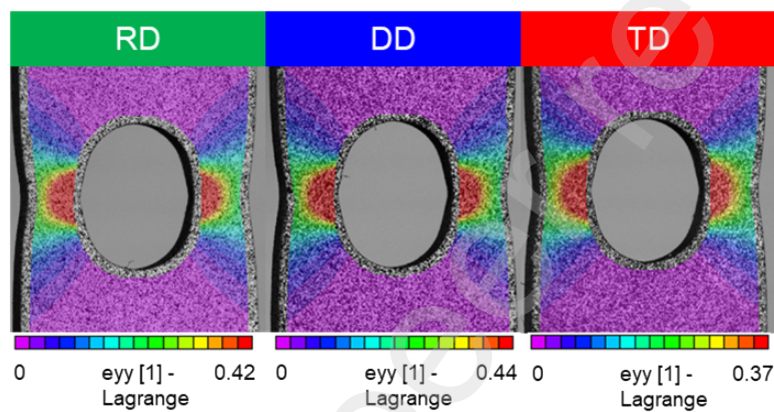
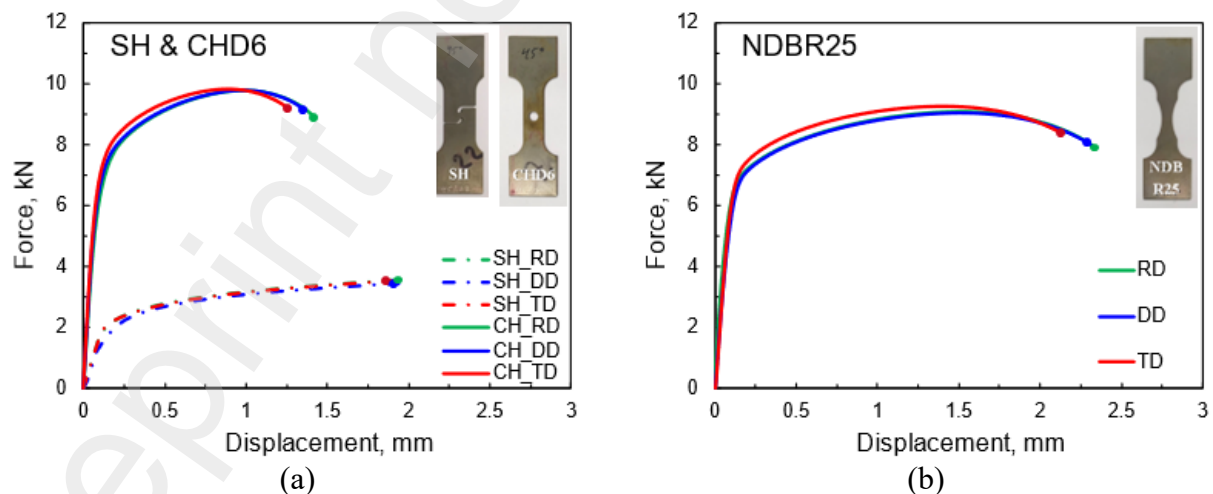


Figure 3: Contour plots of logarithmic axial strain at fracture displacements along three tensile directions on CHD6 specimens.



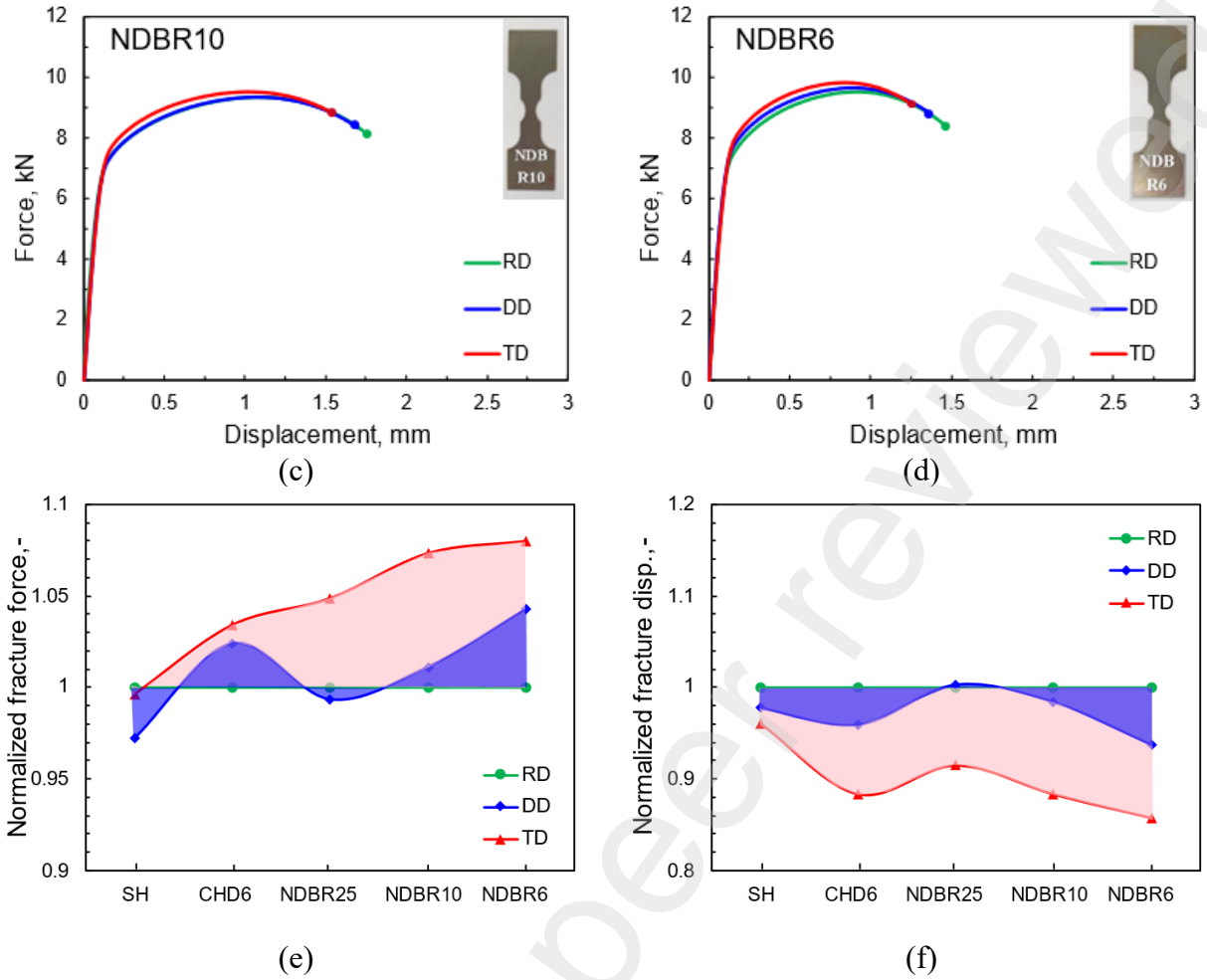


Figure 4: The force–displacement curves of QP1000 on RD, DD, and TD for (a) SH together with CHD6, (b) NDBR25, (c) NDBR10, (d) NDBR6, (e) normalized fracture force, and (f) normalized fracture displacement of DD and TD with respect to RD.

3 Constitutive models

The precise description of plastic flow behavior is an important prerequisite in the successful prediction of stress-state-dependent fracture properties of anisotropic materials. Depending on how the anisotropy effects are coupled in the failure criterion, anisotropic fracture models can be classified as partially [50] and fully anisotropic [51] models. For partially anisotropic models, only the influence from anisotropic plasticity is taken into account, meaning the fracture criterion is isotropic, which showed success for both aluminum alloys [52] and pipeline steels [53]. For fully anisotropic fracture models, the influence of loading direction on the fracture strain [54] or stress [55] is captured by formulating a unified fracture criterion together with an

anisotropic yield criterion.

In partially anisotropic fracture models, the orientation-dependent fracture properties are mainly attributed to the anisotropic plastic flow during deformation. Based on this assumption, the failure criterion parameters are typically calibrated independently for one loading direction, and their applicability to other loading directions needs to be verified. The fully anisotropic fracture models are devoted to formulating a unified criterion that can be applied to arbitrary loading directions, which typically requires the experimental results of fracture tests along three loading directions. Both partially and fully anisotropic approaches have been used to investigate the fracture behavior of QP1000 steel in this study.

3.1 Partially anisotropic fracture model

A partially anisotropic fracture model has been proposed by Shen et al. [56] to describe the fracture properties of high-strength pipeline steels. The partially anisotropic fracture model is formulated by integrating the enHill48 plasticity model [49] into the hybrid damage mechanics framework proposed by Lian et al. [34], which can be flexibly applied for either damage-dominant fracture in modern advanced high-strength steels [57] or damage-negligible fracture [58, 59]. By adopting the non-associated flow rule and considering the evolution of anisotropic stress and r -value, it has been shown that the enHill48 model provides improved accuracy in the final prediction of localization [60] and ductile fracture [56] of different steels.

The yield criterion f and flow potential g are separately defined in the partially anisotropic fracture model, where a scalar parameter D is adopted to quantify the damage-induced softening after reaching the damage initiation criterion.

$$f = \bar{\sigma}_\sigma(\boldsymbol{\sigma}) - (1 - D) \cdot \sigma_Y(\bar{\epsilon}^P) \leq 0 \quad (1)$$

$$g = \bar{\sigma}_r(\boldsymbol{\sigma}) - (1 - D) \cdot \sigma_Y(\bar{\epsilon}^P) \leq 0 \quad (2)$$

where the quadratic Hill48 equivalent stresses $\bar{\sigma}_\sigma(\boldsymbol{\sigma})$, $\bar{\sigma}_r(\boldsymbol{\sigma})$ are calculated as below:

$$\bar{\sigma}_\sigma(\boldsymbol{\sigma}) = \left\{ \frac{1}{2} [F_\sigma(\sigma_{22} - \sigma_{33})^2 + G_\sigma(\sigma_{33} - \sigma_{11})^2 + H_\sigma(\sigma_{11} - \sigma_{22})^2] + L_\sigma\sigma_{23}^2 + M_\sigma\sigma_{13}^2 + N_\sigma\sigma_{12}^2 \right\}^{\frac{1}{2}} \quad (3)$$

$$\bar{\sigma}_r(\sigma) = \left\{ \frac{1}{2} [F_r(\sigma_{22} - \sigma_{33})^2 + G_r(\sigma_{33} - \sigma_{11})^2 + H_r(\sigma_{11} - \sigma_{22})^2] + L_r\sigma_{23}^2 + M_r\sigma_{13}^2 + N_r\sigma_{12}^2 \right\}^{\frac{1}{2}} \quad (4)$$

The onset of plastic deformation is described by the condition when $D = 0$, $f = 0$, and $g = 0$.

The evolution of anisotropy is captured by considering the change of anisotropic parameters with the equivalent plastic strain $\bar{\epsilon}^p$. In the yield function, the anisotropic parameters ($F_\sigma, G_\sigma, H_\sigma, N_\sigma$) are calculated according to stresses determined from uniaxial tension (σ_0, σ_{45} and σ_{90}) and equibiaxial tension σ_b . The anisotropic parameters (F_r, G_r, H_r, N_r) in the flow potential are determined by the r-values. The parameters L and M in both yield function and flow potential are set as 3, assuming only in-plane anisotropy according to Aretz [61].

$$\begin{aligned} F_\sigma &= \frac{\sigma_0^2(\bar{\epsilon}^p)}{\sigma_{90}^2(\bar{\epsilon}^p)} - 1 + \frac{\sigma_0^2(\bar{\epsilon}^p)}{\sigma_b^2(\bar{\epsilon}^p)}, & G_\sigma &= 1 - \frac{\sigma_0^2(\bar{\epsilon}^p)}{\sigma_{90}^2(\bar{\epsilon}^p)} + \frac{\sigma_0^2(\bar{\epsilon}^p)}{\sigma_b^2(\bar{\epsilon}^p)}, \\ H_\sigma &= 1 + \frac{\sigma_0^2(\bar{\epsilon}^p)}{\sigma_{90}^2(\bar{\epsilon}^p)} - \frac{\sigma_0^2(\bar{\epsilon}^p)}{\sigma_b^2(\bar{\epsilon}^p)}, & N_\sigma &= \frac{4 \cdot \sigma_0^2(\bar{\epsilon}^p)}{\sigma_{45}^2(\bar{\epsilon}^p)} - \frac{\sigma_0^2(\bar{\epsilon}^p)}{\sigma_b^2(\bar{\epsilon}^p)}, \end{aligned} \quad (5)$$

$$\begin{aligned} F_r &= \frac{2 \cdot r_0(\bar{\epsilon}^p)}{r_{90}(\bar{\epsilon}^p) \cdot [1 + r_0(\bar{\epsilon}^p)]}, & G_r &= \frac{2}{1 + r_0(\bar{\epsilon}^p)}, \\ H_r &= \frac{2 \cdot r_0(\bar{\epsilon}^p)}{1 + r_0(\bar{\epsilon}^p)}, & N_r &= \frac{2 \cdot [r_0(\bar{\epsilon}^p) + r_{90}(\bar{\epsilon}^p)] \cdot [r_{45}(\bar{\epsilon}^p) + 0.5]}{r_{90}(\bar{\epsilon}^p) \cdot [1 + r_0(\bar{\epsilon}^p)]} \end{aligned} \quad (6)$$

The reference flow curve $\sigma_Y(\bar{\epsilon}^p)$ is obtained from the uniaxial tensile test along RD. The flow curves are described by the combined Swift and Voce hardening law, with hardening parameters ($A, \bar{\epsilon}_0, n, k_0, Q, \beta, \alpha$) calibrated for individual loading directions along RD, DD, TD, and biaxial tension. The evolution of the r-values along three loading directions obtained from uniaxial tensile tests is fitted by the Voce exponential law, with constants ($C_1 \sim C_3$) independently calibrated for each loading direction.

$$\sigma_Y(\bar{\epsilon}^p) = \alpha \cdot A(\bar{\epsilon}_0 + \bar{\epsilon}^p)^n + (1 - \alpha) \cdot [k_0 + Q(1 - e^{-\beta \bar{\epsilon}^p})] \quad (7)$$

$$r(\bar{\epsilon}^p) = C_1 + C_2(1 - e^{-C_3 \bar{\epsilon}^p}) \quad (8)$$

The flow potential g controls the evolving strain components according to the non-associated flow rule with the equivalent plastic strain rate $\dot{\bar{\epsilon}}^p$, which is not equal to the non-negative plastic multiplier $\dot{\lambda}$ as conventional, and it reads:

$$\dot{\boldsymbol{\varepsilon}}^p = \dot{\lambda} \cdot \frac{\partial g}{\partial \boldsymbol{\sigma}} = \dot{\lambda} \cdot \frac{\partial \bar{\sigma}_r}{\partial \boldsymbol{\sigma}} \quad (9)$$

$$\dot{\bar{\varepsilon}}^p = \dot{\lambda} \cdot \frac{\bar{\sigma}_r}{\bar{\sigma}_\sigma} \quad (10)$$

For a detailed derivation of the enHill48 model, the readers are referred to the previous study [49]. For fracture, stress triaxiality and Lode angle (η , $\bar{\theta}$) are widely used for the general characterization of the stress states, which are related to the invariants of the Cauchy stress tensor $\boldsymbol{\sigma}$ and the deviatoric stress tensor \mathbf{s} . These two variables are related to each other under plane stress conditions [17]. For proportional loading conditions, a damage initiation criterion is defined by a critical value of the equivalent plastic strain, and a ductile fracture criterion, which are both dependent on stress triaxiality and Lode angle. The symmetric damage initiation locus (DIL) $\bar{\varepsilon}_{ddi}(\eta, \bar{\theta})$ and ductile fracture locus (DFL) $\bar{\varepsilon}_{df}(\eta, \bar{\theta})$ are described by four parameters ($D_{1\sim4}$ and $F_{1\sim4}$), respectively. A cut-off value of stress triaxiality ($\eta_c = -1/3$) [62] is assumed that the damage and fracture will not be triggered when the stress triaxiality is below η_c ($\bar{\varepsilon}_{ddi}(\eta, \bar{\theta}) = \bar{\varepsilon}_{df}(\eta, \bar{\theta}) = +\infty$, $\eta \leq \eta_c$).

$$\bar{\varepsilon}_{ddi}(\eta, \bar{\theta}) = (D_1 \cdot e^{-D_2 \eta} - D_3 \cdot e^{-D_4 \eta}) \cdot \bar{\theta}^2 + D_3 \cdot e^{-D_4 \eta} \quad (11)$$

$$\bar{\varepsilon}_{df}(\eta, \bar{\theta}) = (F_1 \cdot e^{-F_2 \eta} - F_3 \cdot e^{-F_4 \eta}) \cdot \bar{\theta}^2 + F_3 \cdot e^{-F_4 \eta} \quad (12)$$

When non-proportional loading conditions are concerned, the average values of both stress state variables (η_{avg} , $\bar{\theta}_{avg}$) until the specific point instead of the instantaneous ones are used to represent the general stress states considering the evolution history.

$$\eta_{avg} = \frac{1}{\bar{\varepsilon}} \int_0^{\bar{\varepsilon}} \eta d\bar{\varepsilon}^p \quad (13)$$

$$\bar{\theta}_{avg} = \frac{1}{\bar{\varepsilon}} \int_0^{\bar{\varepsilon}} \bar{\theta} d\bar{\varepsilon}^p \quad (14)$$

The indicator of ductile damage initiation I_{dd} and indicator of ductile fracture I_{df} are applied to quantify the effects of loading paths on damage and fracture. The initiation of damage and fracture occurs when the corresponding indicator reaches the unity. A linear damage

accumulation law is assumed, which is controlled by the equivalent stress at the damage initiation point $\bar{\sigma}_{ddi}$ and the energy dissipation parameter G_f .

$$I_{dd} = \int_0^{\bar{\epsilon}^p} \frac{1}{\bar{\epsilon}_{ddi}(\eta, \bar{\theta})} d\bar{\epsilon}^p \quad (15)$$

$$I_{df} = \int_{\bar{\epsilon}_{ddi}}^{\bar{\epsilon}^p} \frac{1}{\bar{\epsilon}_{df}(\eta, \bar{\theta}) - \bar{\epsilon}_{ddi}(\eta, \bar{\theta})} d\bar{\epsilon}^p \quad (16)$$

$$D = \begin{cases} 0 & I_{dd} < 1 \\ \frac{\bar{\sigma}_{ddi}^c}{G_f} \cdot I_{df} & I_{dd} \geq 1 \quad \wedge \quad I_{df} < 1 \\ 1 & I_{dd} \geq 1 \quad \wedge \quad I_{df} \geq 1 \end{cases} \quad (17)$$

3.2 Fully anisotropic fracture model

To enrich the flexibility in presenting the anisotropy in fracture, the fully anisotropic fracture criteria have been formulated, in which the linear transformation concept from the anisotropic plasticity models, such as Yld2000-2D [63], Yld2004-18p [64], Yld2011-27p [65] has been adopted to unify either the strain components [66] or the stress components [67]. Recently, a scaling method by formulating the fracture parameters as a function of loading angles has also been proposed and applied to steels [68] and aluminum alloys [69].

In this study, the fully anisotropic fracture model manipulating the strain components based on linear transformation is employed. For any arbitrary stress state, the plastic strain rate tensor $\dot{\epsilon}^p$ contains five independent components considering the incompressibility of plastic deformation. The anisotropy effects are described by the transformation tensor \mathbf{C} , which is identical to the one in the Yld2004 plasticity model. The plastic incompressibility is considered by using the modified transformation tensor \mathbf{T} , following the recommendation by Lou and Yoon [66]. The anisotropic strain rate tensor $\dot{\epsilon}$ is formulated by applying the linear transformation \mathbf{L} to the plastic strain rate tensor $\dot{\epsilon}^p$.

$$\dot{\epsilon} = \mathbf{C} \cdot \mathbf{T} \cdot \dot{\epsilon}^p = \mathbf{L} \cdot \dot{\epsilon}^p \quad (18)$$

$$\mathbf{C} = \begin{bmatrix} 0 & -c_{12} & -c_{13} & 0 & 0 & 0 \\ -c_{21} & 0 & -c_{23} & 0 & 0 & 0 \\ -c_{31} & -c_{32} & 0 & 0 & 0 & 0 \\ 0 & 0 & 0 & c_{44} & 0 & 0 \\ 0 & 0 & 0 & 0 & c_{55} & 0 \\ 0 & 0 & 0 & 0 & 0 & c_{66} \end{bmatrix}; \mathbf{T} = \begin{bmatrix} 1 & 0 & 0 & 0 & 0 \\ 0 & 1 & 0 & 0 & 0 \\ -1 & -1 & 0 & 0 & 0 \\ 0 & 0 & 1 & 0 & 0 \\ 0 & 0 & 0 & 1 & 0 \\ 0 & 0 & 0 & 0 & 1 \end{bmatrix} \quad (19)$$

Hence the components of $\dot{\mathbf{e}}$ are calculated as:

$$\dot{\mathbf{e}} = \begin{bmatrix} \dot{\epsilon}_{11}^a \\ \dot{\epsilon}_{22}^a \\ \dot{\epsilon}_{33}^a \\ \dot{\epsilon}_{23}^a \\ \dot{\epsilon}_{13}^a \\ \dot{\epsilon}_{12}^a \end{bmatrix} = \mathbf{L} \cdot \dot{\mathbf{\epsilon}}^p = \begin{bmatrix} c_{13} & -c_{12} + c_{13} & 0 & 0 & 0 \\ -c_{21} + c_{23} & c_{23} & 0 & 0 & 0 \\ -c_{31} & -c_{32} & 0 & 0 & 0 \\ 0 & 0 & c_{44} & 0 & 0 \\ 0 & 0 & 0 & c_{55} & 0 \\ 0 & 0 & 0 & 0 & c_{66} \end{bmatrix} \cdot \begin{bmatrix} \dot{\epsilon}_{11}^p \\ \dot{\epsilon}_{22}^p \\ \dot{\epsilon}_{23}^p \\ \dot{\epsilon}_{13}^p \\ \dot{\epsilon}_{12}^p \end{bmatrix} \quad (20)$$

When all the anisotropic parameters c_{ij} take the value of one, then the model is reduced to isotropic. The corresponding anisotropic equivalent strain rate $\dot{\bar{\epsilon}}^a$ of the anisotropic strain rate tensor $\dot{\mathbf{e}}$ is determined according to expression in the classical Mises plasticity theory:

$$\dot{\bar{\epsilon}}^a = \sqrt{\frac{2}{3}} \dot{\mathbf{e}} : \dot{\mathbf{e}} \quad (21)$$

The anisotropic ductile failure criteria are formulated as a critical value of the anisotropic equivalent strain at the ductile damage initiation $\bar{\epsilon}_{\text{ddi}}^a$, and ductile fracture $\bar{\epsilon}_{\text{df}}^a$, which depend on the stress states whereas independent of loading orientations.

$$\bar{\epsilon}_{\text{ddi}}^a(\eta, \bar{\theta}) = (D_1^a \cdot e^{-D_2^a \eta} - D_3^a \cdot e^{-D_4^a \eta}) \cdot \bar{\theta}^2 + D_3^a \cdot e^{-D_4^a \eta} \quad (22)$$

$$\bar{\epsilon}_{\text{df}}^a(\eta, \bar{\theta}) = (F_1^a \cdot e^{-F_2^a \eta} - F_3^a \cdot e^{-F_4^a \eta}) \cdot \bar{\theta}^2 + F_3^a \cdot e^{-F_4^a \eta} \quad (23)$$

$D_{1 \sim 4}^a$ and $F_{1 \sim 4}^a$ are material parameters to be calibrated for the anisotropic damage initiation locus and ductile fracture locus, respectively. Two different sets of anisotropic parameters c_{ij} can be determined for damage initiation and ductile fracture criteria using experimental results under different stress states and loading orientations. Similar to the isotropic formulation, the indicator of anisotropic damage initiation I_{dd}^a and anisotropic ductile fracture I_{df}^a are used for non-proportional loading conditions, as shown in Eq. 24-25. Based on the formulated

anisotropic loci, it is assumed that damage evolution is independent of loading directions, i.e., the energy dissipation parameter G_f stays as a constant.

$$I_{dd}^a = \int_0^{\bar{\varepsilon}^p} \frac{1}{\bar{\varepsilon}_{ddi}^a(\eta, \bar{\theta})} d\bar{\varepsilon}^a \quad (24)$$

$$I_{df}^a = \int_{\bar{\varepsilon}_{ddi}^a}^{\bar{\varepsilon}^a} \frac{1}{\bar{\varepsilon}_{df}^a(\eta, \bar{\theta}) - \bar{\varepsilon}_{ddi}^a(\eta, \bar{\theta})} d\bar{\varepsilon}^a \quad (25)$$

$$D = \begin{cases} 0 & I_{dd} < 1 \\ \frac{\bar{\sigma}_{ddi}^c}{G_f} \cdot I_{df}^a & I_{dd} \geq 1 \quad \wedge \quad I_{df} < 1 \\ 1 & I_{dd} \geq 1 \quad \wedge \quad I_{df} \geq 1 \end{cases} \quad (26)$$

4 Plasticity parameters calibration and validation

4.1 Anisotropic plasticity parameters calibration

The anisotropy of the material plasticity evolves in terms of both stress and r-value during plastic deformation. The strain hardening behavior of QP1000 is described using the combined Swift-Voce hardening law, where the individual parameters for each loading condition are fitted based on experimental stress–strain curves, as shown in Figure 5 (a). The r-value curves from three uniaxial tension directions are fitted by Voce law to capture the anisotropic evolving feature as depicted in Figure 5 (b). To illustrate the pattern of the anisotropic evolution, normalized stress and r-values at yielding points (approximately strain level of 0.002), 0.02, 0.05, the onset of necking (approximately strain level of 0.15), and at larger strain (0.5) are plotted in Figure 5 (c) and (d). From the results, it is observed that the anisotropic pattern of r-value distribution over loading direction is amplified with increased plastic strain, which necessitates the application of evolving plasticity models. Both the yield locus and flow potential are evolving during plastic deformation, as shown in Figure 5 (e) and (f) at strain levels of 0.002, 0.05, and 0.5, together with Mises as a reference. The evolving characteristics of anisotropy can be well captured by the enHill48 anisotropic plasticity model. The calibrated

parameters for hardening and r-values are listed in Table 3 and Table 4.

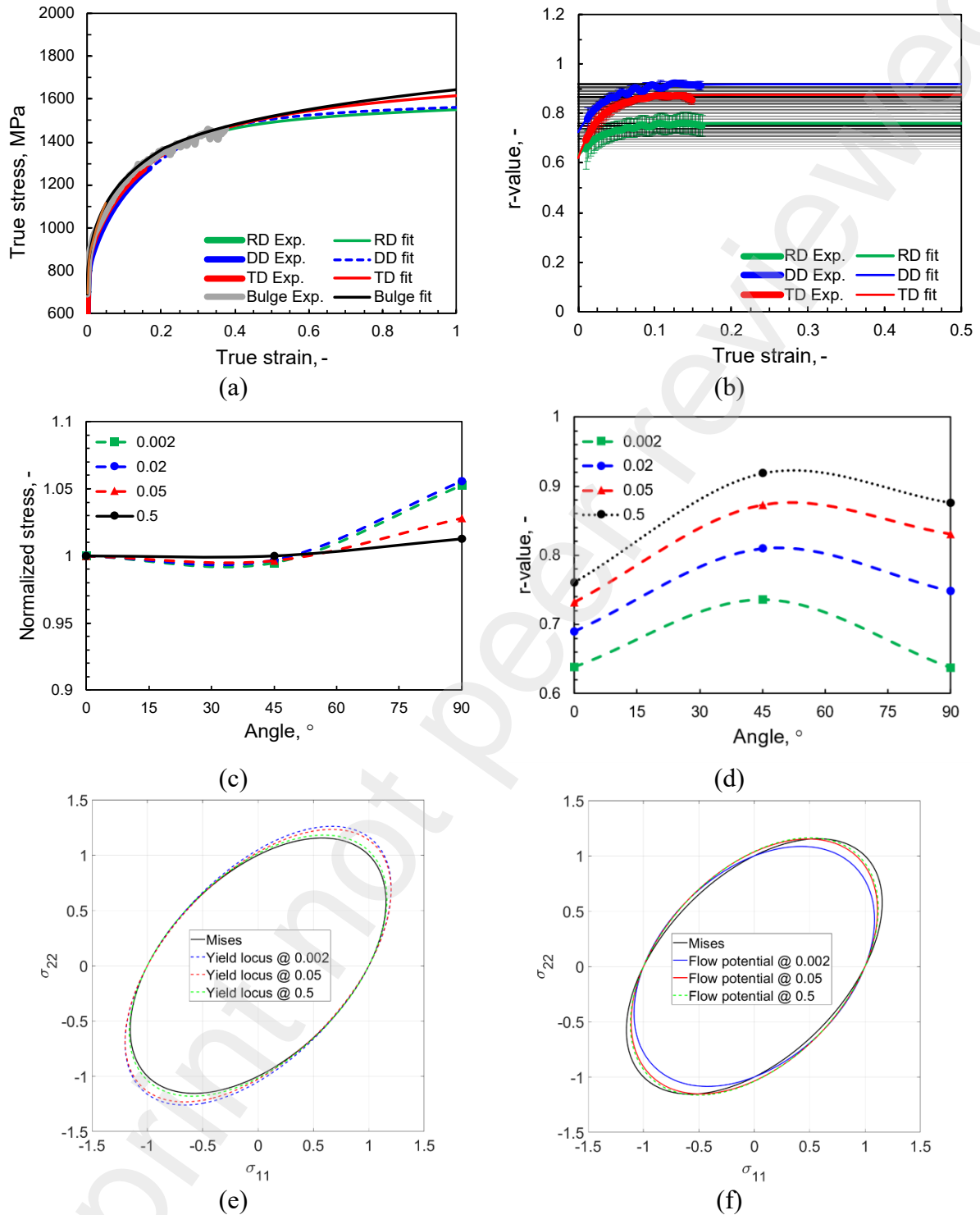


Figure 5: The flow stress and r-value evolution from tests and model calibration: (a) true stress–strain curves of tensile tests along three loading directions and Bulge test with extrapolation using piecewise Swift-Voce law, (b) r-value evolution curves of tensile tests along three loading directions fitted by Voce law, (c) directionality of the normalized stress, (d) r-value, (e) yield locus and (f) flow potential at different strain levels from the enHill48 model.

Table 3: Calibrated parameters in hardening functions for the flow curve extrapolation.

Plastic strain range	Directions	$\sigma = w \cdot \sigma_{\text{Swift}} + (1 - w) \cdot \sigma_{\text{Voce}}$						
		$\sigma_{\text{Swift}} = A \cdot (\varepsilon_0 + \bar{\varepsilon}^p)^n$			$\sigma_{\text{Voce}} = k_0 + Q \cdot (1 - \exp(-\beta \cdot \bar{\varepsilon}^p))$			
		A	ε_0	n	k_0	Q	β	w
$\bar{\varepsilon}^p \leq 0.02$	RD	1303	2e-5	0.10	0.5	1125	1197	0.85
	DD	1295	4e-5	0.11	0.2	1346	1546	0.86
	TD	1320	1e-5	0.10	0.3	1286	1410	0.87
	Biaxial	2616	0.04	0.38	0.1	1700	423	0.91
$\bar{\varepsilon}^p > 0.02$	RD	1766	6e-5	0.06	0.7	1225	7	0.60
	DD	1606	3e-5	0.07	0.7	1442	7	0.66
	TD	1598	0.01	0.10	0.8	1686	6	0.81
	Biaxial	1722	0.5	0.12	0.5	1195	10	0.52

Table 4: Calibrated parameters in Voce law for r-value curve extrapolation.

Constants	$r_{\text{Voce}}(\bar{\varepsilon}^p) = C_1 + C_2(1 - e^{-C_3\bar{\varepsilon}^p})$		
	C_1	C_2	C_3
r_{0°	0.63	0.13	30.26
r_{45°	0.73	0.19	28.74
r_{90°	0.62	0.26	34.59

4.2 Anisotropic plasticity parameters validation

To validate the plasticity model, finite element (FE) simulations of uniaxial tension with five geometries along three directions are performed. Since the deformation is mainly concentrated around the notch area, the half-thickness FE models (due to in-plane anisotropy) corresponding to the extensometer measurement region of the specimens are built to increase the computational efficiency. First-order reduced-integration solid elements (C3D8R from Abaqus) with the size of 0.05 mm in three directions are used to capture the deformation around the critical area, while the rest part of the model is featured with a coarser mesh. The constitutive

model is implemented via a VUMAT user material subroutine in Abaqus/Explicit.

The performance of the anisotropic plasticity model is firstly validated based on the force–displacement responses predicted by the numerical simulations and the experimental results in each direction, as shown in Figure 6 (a). The anisotropic plasticity model provides accurate prediction of force–displacement curves until the fracture points in all three directions during plastic deformation. The prediction quality is especially high for CH and NDB specimens with large radii in both the uniform deformation and post-necking deformation towards the end. In addition, a high agreement with experimental results is achieved by the plasticity model in the description of local strain fields. Virtual extensometers with a length of 1 mm are placed across the fracture region for both the DIC reference image and the FE model. Local strain is measured along the virtual extensometer and compared between FE simulation and experimental results, as shown in Figure 6 (b). The prediction on the history of nominal strain until fracture matches well with DIC results for different geometries and loading directions. The enHill48 model shows a good capability in accurately describing both the anisotropic plasticity and the anisotropic evolving features of the investigated QP1000 steel.

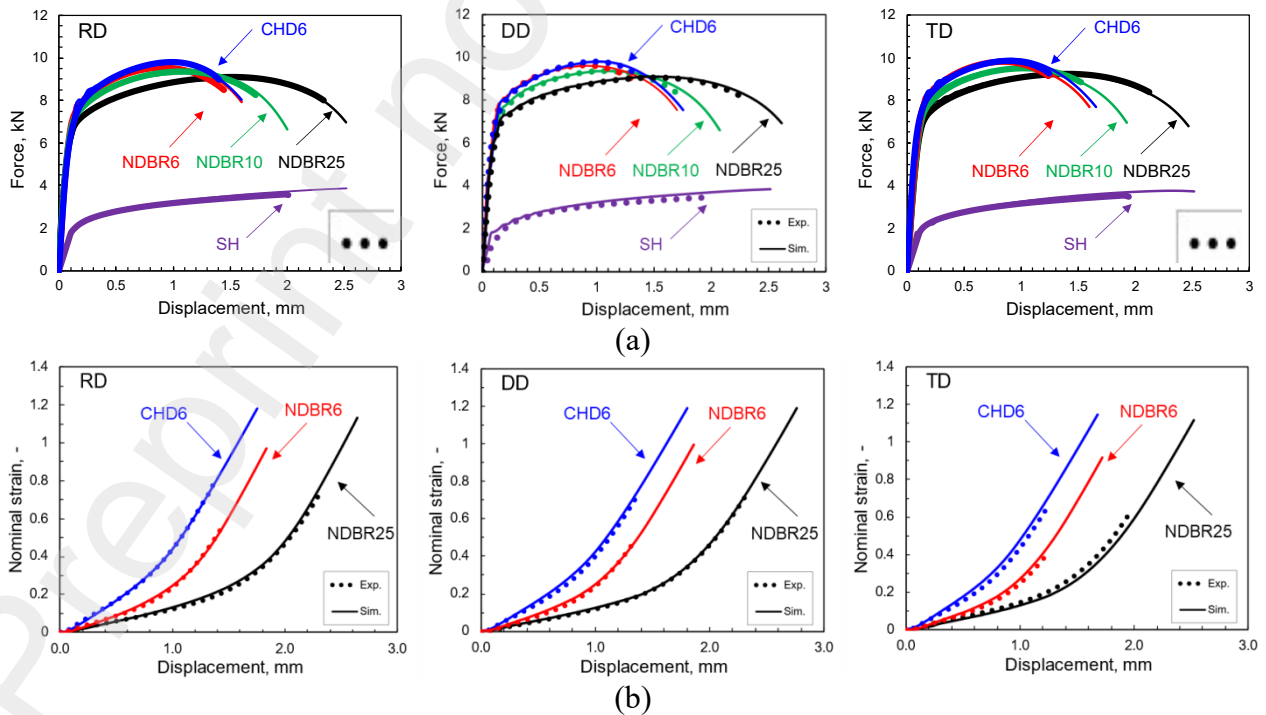


Figure 6: Validation of the anisotropic plasticity model compared with experimental results of

tensile tests in RD, DD, and TD on (a) the force–displacement curves, and (b) the evolution of nominal strain.

5 Partially anisotropic approaches

5.1 Calibration and validation of partially anisotropic fracture model

Based on the failure mechanisms analysis of the fracture surfaces in [16], the damage initiation in QP1000 takes place at a rather late stage of plastic deformation with a rapid damage evolution. Therefore, the uncoupled damage mechanics approach flexibly offered by the HDM model [34] is employed for this QP1000 steel by taking the critical strain values at fracture points (corresponding to the sudden force drop) to determine the damage initiation parameters ($D_{1\sim4}$) and assuming the DIL converges with the DFL. Therefore, the two sets of damage/fracture parameters are reduced to only the four damage initiation parameters. In addition, the damage evolution parameter G_f is also omitted due to the uncoupled use of the HDM model for rapid damage evolution.

With one set of plasticity parameters determined for the QP1000 steel for all loading directions, the damage initiation parameters ($D_{1\sim4}$) in the partially anisotropic fracture model have been calibrated separately for RD and TD based on the local stress and strain variables in critical elements extracted from simulations, as listed in Table 5. The locations of the critical elements were shown in detail in the previous investigation [35]. It is evident that in Figure 7 the local stress state in the critical elements of all specimens is rather not constant during deformation. Therefore, the values of local stress state variables (η_{avg} , $\bar{\theta}_{avg}$) are averaged along deformation until the fracture moment, shown as solid dots in Figure 7 (b)-(d), to represent the overall stress state and characterize non-proportional loading effects. The calibrated fracture parameters for RD and TD are shown in Figure 7. The two ductile fracture loci for RD and TD are constructed in the 3D space of equivalent plastic strain (PEEQ), stress triaxiality, and Lode angle parameter in Figure 7 (a), with the plane stress conditions relevant for sheet metal forming highlighted by

a solid curve.

Noticeable anisotropic effects on the fracture condition have been observed for the investigated QP1000 steel. It is noticed that the impacts of the stress state on fracture are significantly affected by the loading direction. For each Lode angle value, the stress triaxiality has a more pronounced influence on the failure strain in TD than RD. Similarly, the failure strain in TD is more sensitive to the Lode angle than RD for a given stress triaxiality. In particular, the anisotropic effect on damage/failure strain is enhanced with increasing stress triaxiality. The performance of the partially anisotropic fracture model in predicting the global force–displacement response for all five fracture specimens is presented in Figure 8. The experimental (dotted curves) and numerical (solid curves) results of force–displacement response in tensile tests are represented by green and red curves for RD and TD, respectively. The fracture points from experimental data are marked with the corresponding-colored quadrilaterals for each direction. When the independently determined fracture criterion for RD and TD is applied to predict the fracture behavior along the corresponding direction, very accurate predictions of fracture force and displacements can be achieved using the partially anisotropic fracture model.

Table 5: The local stress state variables and equivalent plastic strain at the fracture moment.

Loading direction	Specimen	PEEQ	η_{avg}	$\bar{\theta}_{avg}$
RD	SH	0.76	0.04	0.08
	CHD6	0.96	0.32	0.93
	NDBR25	0.85	0.51	0.61
	NDBR10	0.79	0.54	0.50
	NDBR6	0.76	0.57	0.41
DD	SH	0.78	0.04	0.08
	CHD6	0.82	0.33	0.95
	NDBR25	0.83	0.53	0.66
	NDBR10	0.70	0.55	0.57
	NDBR6	0.55	0.55	0.57
TD	SH	0.80	0.05	0.06
	CHD6	0.82	0.33	0.95
	NDBR25	0.61	0.45	0.71
	NDBR10	0.55	0.48	0.60
	NDBR6	0.50	0.51	0.50

Table 6: Calibrated damage initiation parameters of QP1000 in the partially anisotropic fracture model for RD and TD.

Loading direction	D_1	D_2	D_3	D_4
RD	1.03	0.10	0.81	0.10
TD	1.04	0.40	0.86	1.50

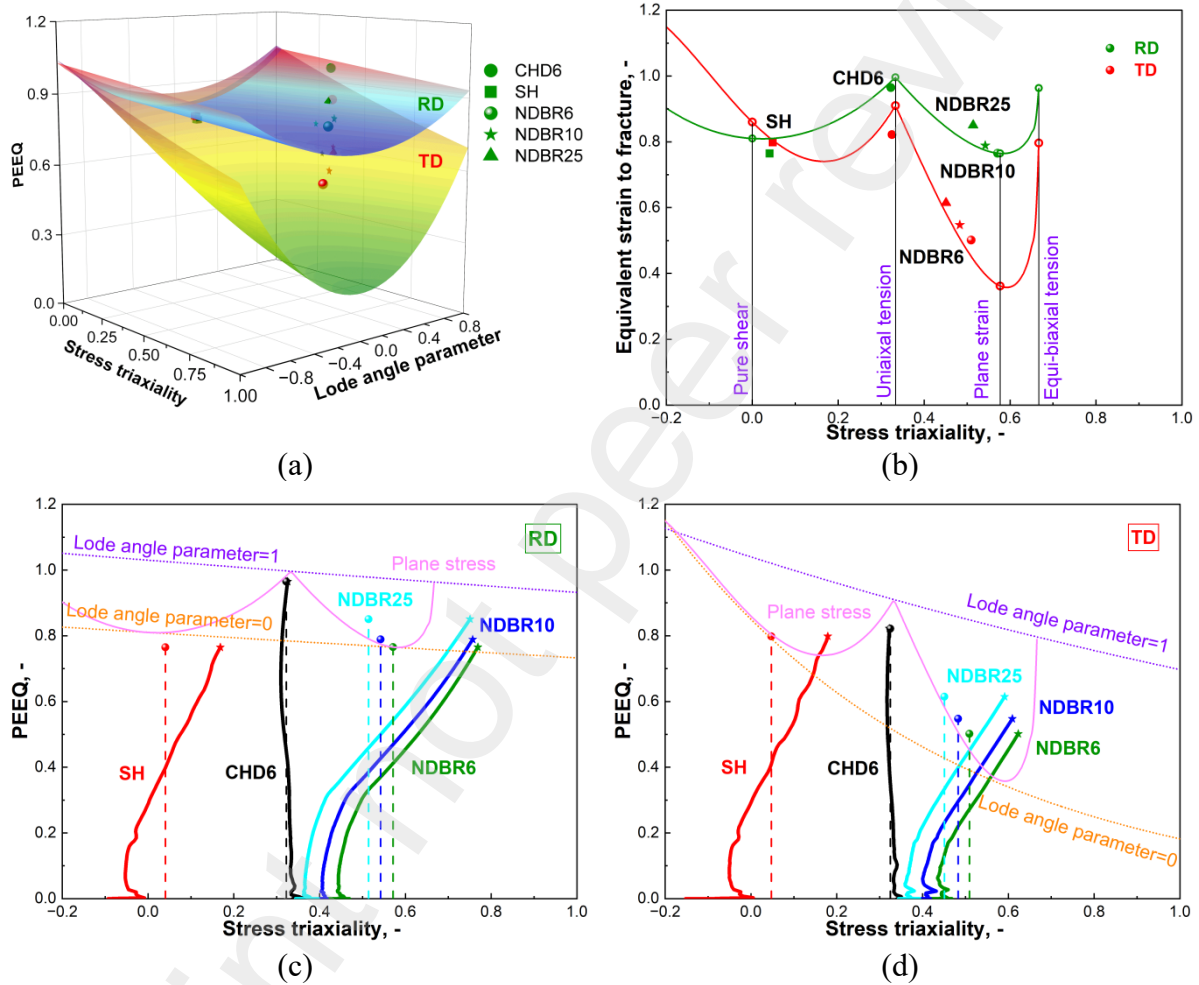


Figure 7: The 3D damage initiation loci (a) in the partially anisotropic fracture model, (b) the fracture strain at stress states of shear, uniaxial tension, plane strain, biaxial tension, the 2D projection of the damage initiation loci with loading paths for (c) RD and (d) TD, in which the cross indicates the fracture points and the dots are corresponding to the averaged values.

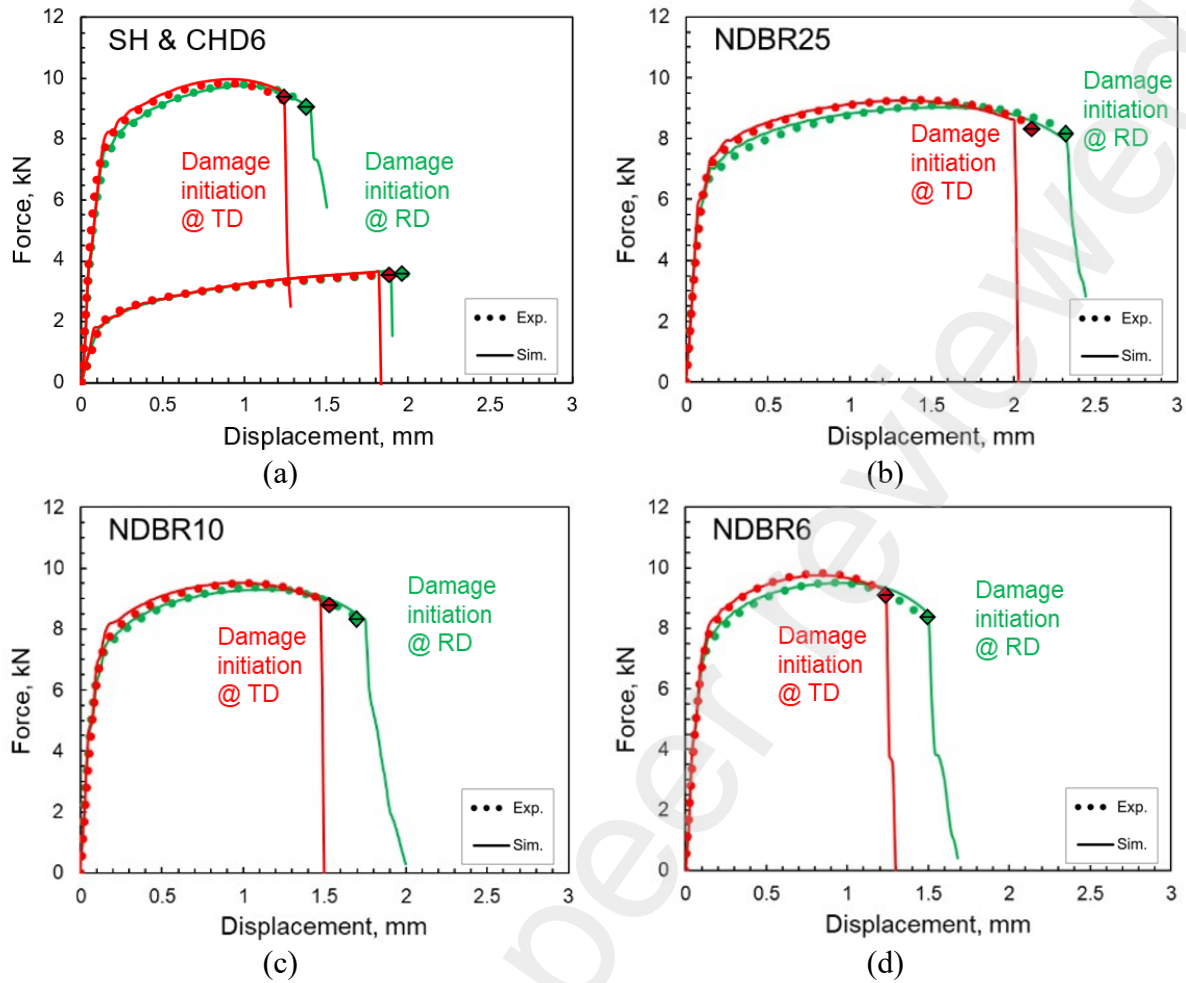


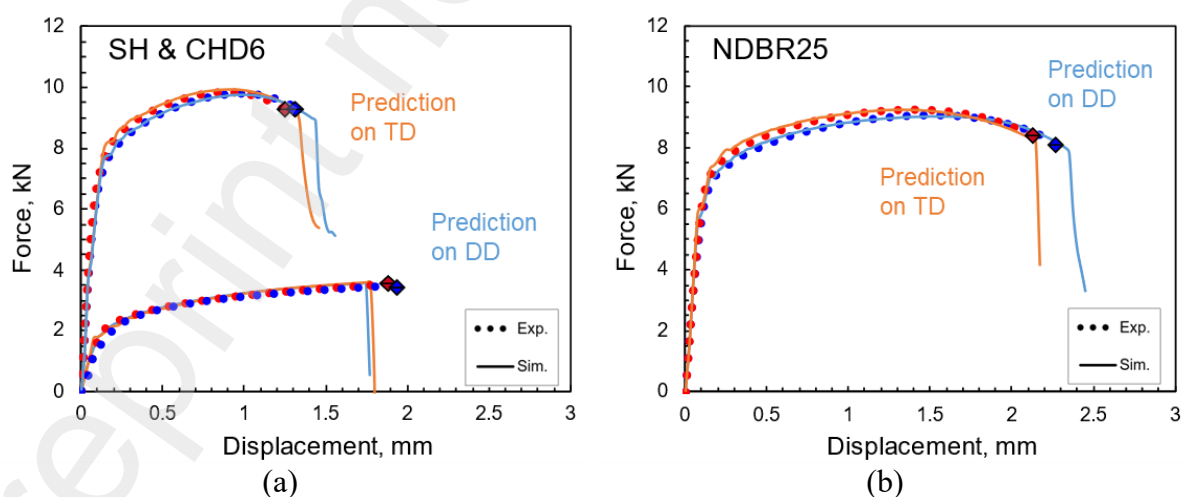
Figure 8: Failure prediction in tensile tests of QP1000 using partially anisotropic fracture model with independently calibrated damage initiation criterion for RD and TD in (a) SH and CHD6, (b) NDBR25, (c) NDBR10, and (d) NDBR6.

5.2 Limitations of partially anisotropic approaches

The limitations of partially anisotropic fracture models are mainly located in the blind prediction of fracture behavior in arbitrary loading directions, which are not involved in parameter calibration. These observed strong variations of failure strain with loading direction indicate that significant deviations will be obtained when using the failure criterion determined for one specific direction to predict the fracture behavior along other loading directions, even for materials showing minor anisotropic effects in the plastic flow behavior. Cross-prediction using the partially anisotropic fracture model with different fracture criteria has been performed to elaborate on the limitations of partially anisotropic approaches. In the first cross-evaluation,

the fracture criterion of the RD is applied to predict the fracture behavior along TD and DD in tensile tests, which is adopted in many investigations on fracture properties of anisotropic materials. As shown in Figure 9, a significant overestimation of the fracture displacements is observed in all geometries (except shear) along other directions when only the failure criterion of the RD is applied. Noticeable underestimation of fracture displacements is obtained in the second cross-evaluation, as shown in Figure 10, where the failure criterion of TD is used to predict the fracture in other loading directions (RD and DD).

To quantify the prediction accuracy of the partially anisotropic fracture model, the predicted fracture displacements of different specimens are normalized by experimental results. The normalized fracture displacements using fracture criteria determined based on RD and TD are shown in Figure 11 (a) and (b), respectively. In the blind predictions on fracture displacements along DD, either significant overestimation or underestimation is obtained using the partially anisotropic fracture model from either RD or TD. It is concluded that for material with minor or moderate plastic anisotropy but pronounced anisotropic fracture behavior, the partially anisotropic fracture models that rely only on the plasticity anisotropy with an isotropic fracture criterion fail to fully describe the anisotropic fracture behavior.



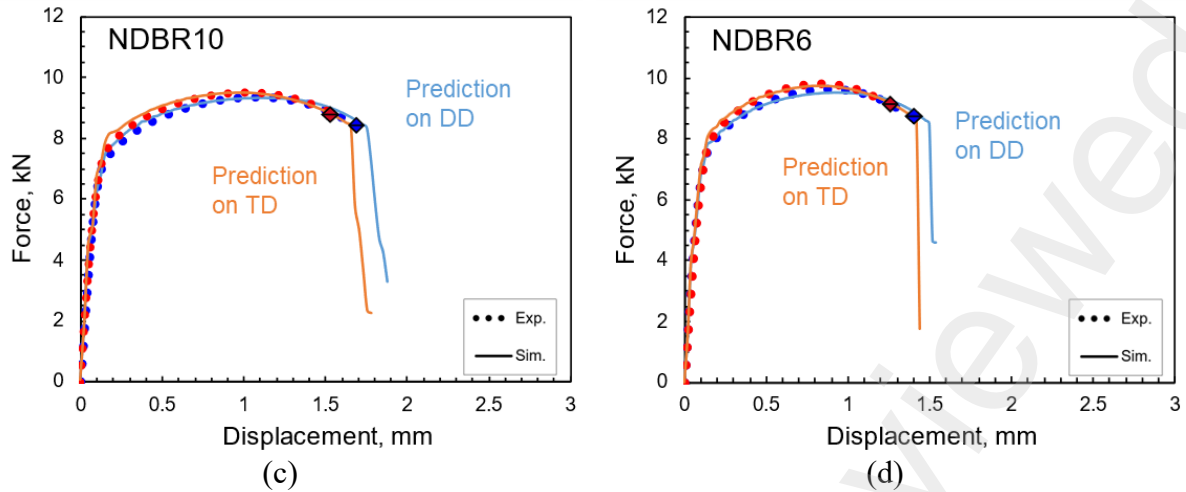


Figure 9: Prediction of fracture in specimens loaded along DD and TD using the partially anisotropic fracture model with failure criterion determined based on RD in (a) SH and CHD6, (b) NDBR25, (c) NDBR10, and (d) NDBR6.

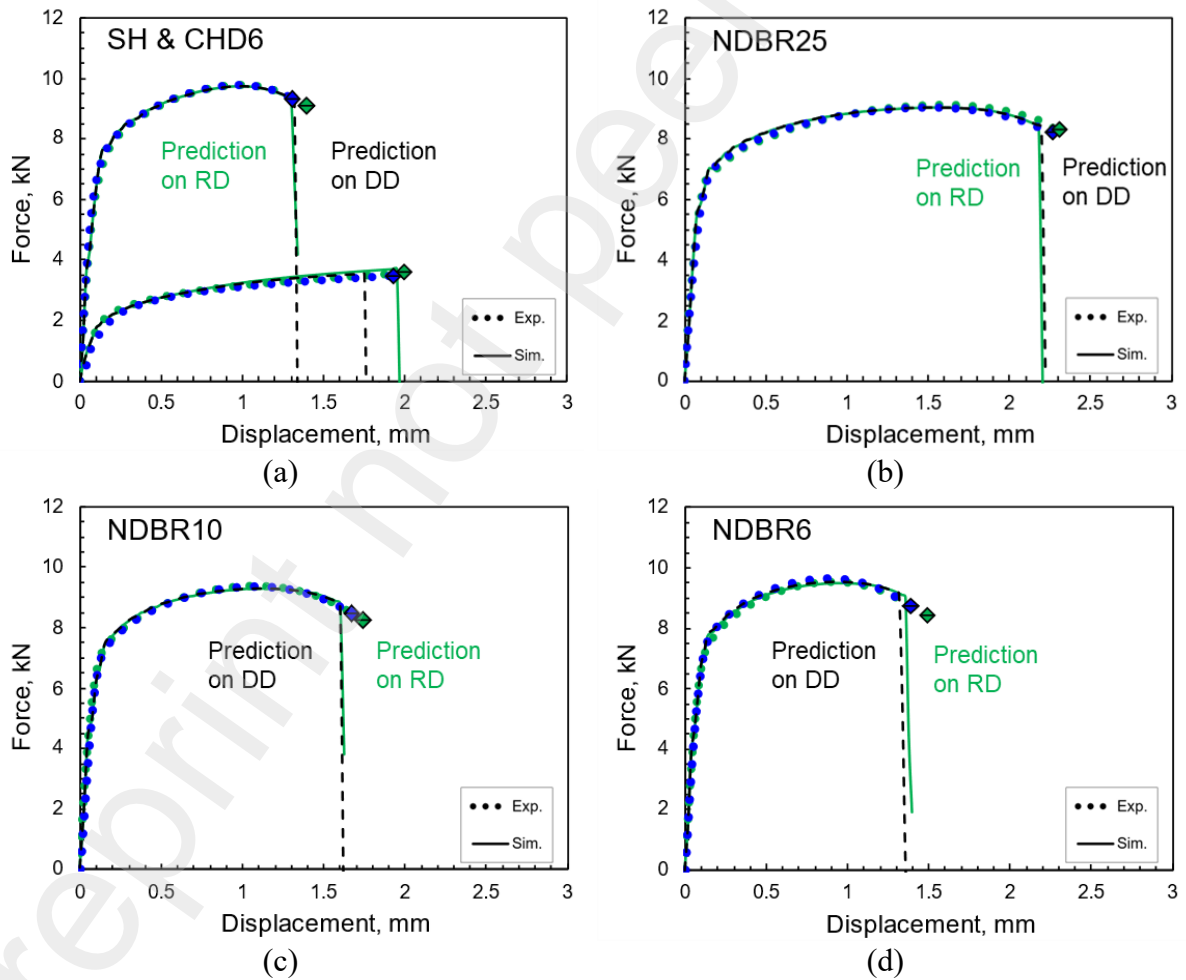


Figure 10: Prediction of fracture in specimens loaded along RD and DD using the partially anisotropic fracture model with failure criterion determined based on TD in (a) SH and CHD6, (b) NDBR25, (c) NDBR10, and (d) NDBR6.

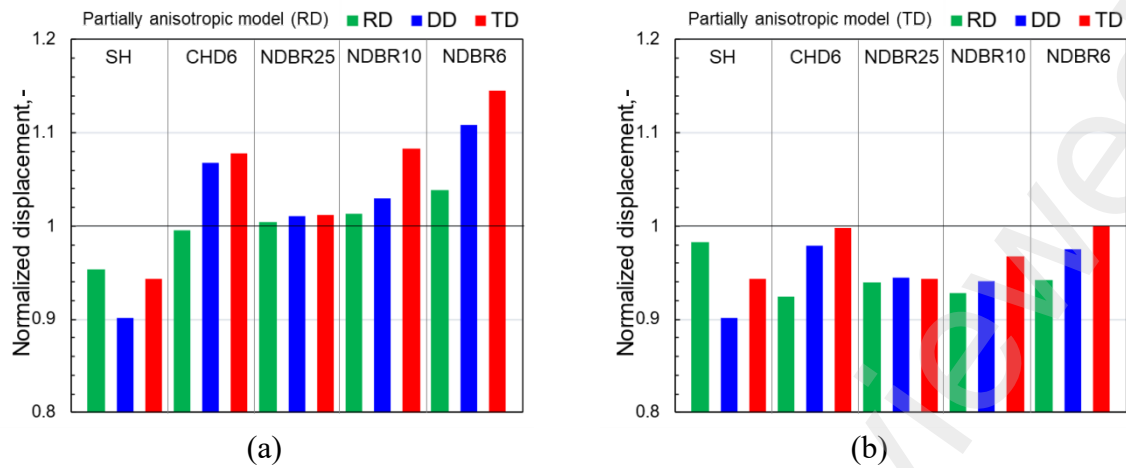


Figure 11: Evaluation of the prediction capacity of the partially anisotropic fracture model based on predicted normalized fracture displacements using damage criterion of (a) RD and (b) TD.

6 Fracture modeling using fully anisotropic criterion

6.1 Parameters calibration of fully anisotropic criterion

Similar to the partially anisotropic fracture model, the fully anisotropic damage mechanics model is simplified to an uncoupled approach by assuming the damage initiation is identical to the ductile fracture. The main advantage of a fully anisotropic criterion lies in its capacity to predict fracture properties along arbitrary loading directions. To demonstrate and evaluate the performance of fully anisotropic fracture criterion, the anisotropic fracture behavior has been predicted using two different parameter calibration strategies. In the first strategy, the local stress and strain values obtained from RD and TD are used to determine anisotropic fracture parameters, referred to as the 2D case. In the second strategy, the strain and strain data of all three loading directions (RD, DD, and TD) are used to calibrate the anisotropic damage parameters, referred to as the 3D case.

The full plastic strain tensor with six components in the critical elements at the crack initiation instant has been collected from each specimen and in individual directions. A linear transformation is applied to the plastic strain rate tensor $\dot{\epsilon}^p$ to obtain the anisotropic strain rate

tensor $\dot{\epsilon}$ according to Eq. (18). The corresponding anisotropic equivalent strain $\bar{\epsilon}^a$ after linear transformation is determined for each specimen and loading direction according to Eq. (19). These anisotropic equivalent strain $\bar{\epsilon}^a$ together with the corresponding stress state variables $(\eta_{avg}, \bar{\theta}_{avg})$ listed in Table 5 are taken as inputs to determine the parameters of the fully anisotropic fracture criterion, including parameters c_{ij} in the linear transformation tensor and four parameters $D_{1\sim4}^a$ in the anisotropic damage initiation locus. An optimization algorithm has been used to minimize the deviation between the linear transformed values of anisotropic equivalent strain and the predicted ones on the anisotropic damage initiation locus. For such an optimization problem, the objective function is defined to be minimized:

$$err = \frac{1}{N} \sum_1^N \left(\frac{\bar{\epsilon}_{Pred.}^a(\eta_{avg}, \bar{\theta}_{avg})}{\bar{\epsilon}_{Tran.}^a(\eta_{avg}, \bar{\theta}_{avg})} - 1 \right)^2 \quad (27)$$

In the objective function, N is the number of data points used for parameter calibration. With five fracture specimens used in this study, the total number of data points is 10 and 15 in the 2D and 3D calibration cases, respectively. The number of parameters c_{ij} to be determined in the linear transformation tensor according to the first strategy (2D case) is reduced to 6 with the symmetry assumption, $c_{21} = c_{12}$, $c_{31} = c_{13}$ and $c_{32} = c_{23}$, which results in 10 parameters to calibrate. For the 3D case, the 9 parameters in the transformation tensors all take independent values, and together with the failure parameters, there are all 13 parameters to calibrate. The two sets of calibrated parameters are listed in Table 7 and Table 8. The corresponding anisotropic fracture strain values are listed in Table 9 and Table 10, in which $\bar{\epsilon}_{Tran.}^a(\eta_{avg}, \bar{\theta}_{avg})$ is the anisotropic equivalent strain after linear transformation and $\bar{\epsilon}_{Pred.}^a(\eta_{avg}, \bar{\theta}_{avg})$ is the predicted value on the anisotropic damage initiation locus for the corresponding stress states. A relatively low error ($err = 0.072$) is achieved in both sets of parameters.

The anisotropic damage initiation locus determined based on two different strategies is constructed for the investigated material. The fully anisotropic damage initiation locus

determined based on all five geometries of three loading directions in the space of anisotropic equivalent strain, stress triaxiality, and Lode angle parameter, are shown in Figure 12. The anisotropic equivalent strain after linear transformation is represented by distinct solid symbols with different colors for each loading direction. In general, a good fitting quality of the anisotropic failure criterion is achieved for RD and TD in both calibration strategies. However, there is a noticeable difference between the damage initiation loci.

Table 7: Calibrated parameters in the fully anisotropic fracture model based on inputs of RD and TD.

c_{12}	c_{13}	c_{21}	c_{23}	c_{31}	c_{32}	c_{44}	c_{55}	c_{66}
1.03	0.71	1.03	0.85	0.71	0.85	0.72	0.70	0.40
C_1^a	C_2^a	C_3^a	C_4^a					
1.00	0.45	0.78	0.55					

Table 8: Calibrated parameters in the fully anisotropic fracture model based on inputs of three directions.

c_{12}	c_{13}	c_{21}	c_{23}	c_{31}	c_{32}	c_{44}	c_{55}	c_{66}
0.11	0.25	1.52	1.07	1.59	1.10	2.16	1.36	0.50
C_1^a	C_2^a	C_3^a	C_4^a					
1.00	0.45	0.78	0.55					

Table 9: The summary of anisotropic damage initiation strain after linear transformation based on inputs of RD and TD.

Loading direction	$\bar{\epsilon}^a$	SH	CHD6	NDBR25	NDBR10	NDBR6
RD	Tran.	0.75	0.85	0.67	0.59	0.51
	Pred.	0.74	0.85	0.67	0.62	0.62
TD	Tran.	0.74	0.84	0.77	0.58	0.48
	Pred.	0.74	0.85	0.68	0.66	0.64

Table 10: The summary of anisotropic damage initiation strain after linear transformation based on inputs of three directions.

Loading direction	$\bar{\epsilon}^a$	SH	CHD6	NDBR25	NDBR10	NDBR6
-------------------	--------------------	----	------	--------	--------	-------

RD	Tran.	0.75	0.81	0.71	0.66	0.58
	Pred.	0.74	0.85	0.67	0.62	0.62
DD	Tran.	0.72	0.84	0.85	0.73	0.57
	Pred.	0.74	0.84	0.67	0.64	0.64
TD	Tran.	0.74	0.84	0.84	0.66	0.55
	Pred.	0.74	0.85	0.68	0.66	0.64

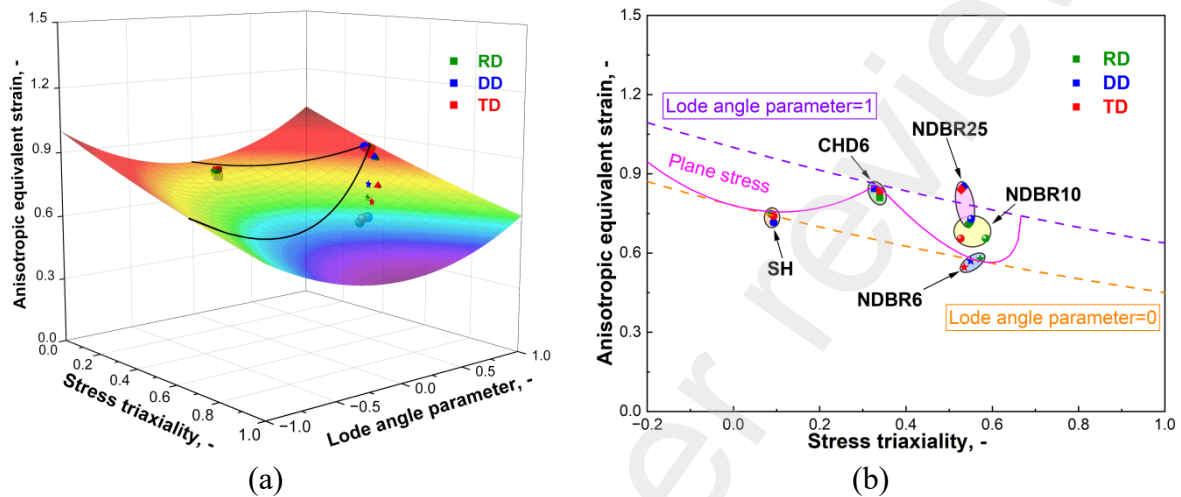


Figure 12: The fully anisotropic damage initiation locus determined based on inputs of all three loading directions, together with the scatter points of RD and TD after linear transformation (a) in 3D, and (b) the 2D projection.

6.2 Evaluation of fully anisotropic fracture criterion

The performance of the fully anisotropic fracture criterion calibrated using two different strategies, in predicting the global force–displacement response for five fracture specimens along three directions is depicted in Figure 14 and Figure 13, respectively. The experimental (dotted) and numerical (line) results are represented by three colors for RD (green), DD (blue), and TD (red) respectively. The fracture points indicated with different color quadrilaterals correspond to the fracture points determined from experiments for each direction. For all specimens tested along RD and TD, the fracture properties are accurately predicted using the fully anisotropic fracture criterion with two different parameter calibration strategies. The fracture displacements in specimens along DD are overestimated by the fully anisotropic fracture criterion, where the local strain/stress values of DD have not been taken in the calibration of the parameters. By comparing the performance of fracture prediction along DD,

it is noticed that the calibration strategy in the 3D case enhanced the performance, and it can be concluded that the accuracy of the fully anisotropic fracture criterion can be improved by including more data points in the calibration procedures.

The overall performance of the fully anisotropic fracture model with two different parameter calibration strategies is quantified in Figure 15. The normalized fracture displacement and force from simulation results of all specimens serve as strong evidence of the significance of parameter calibration strategies on the prediction capacity of the failure models. The fully anisotropic fracture model, calibrated based on inputs of three loading directions, is proven to give accurate predictions on the ductile fracture behavior of QP1000 over a broad range of stress states and loading directions, where non-proportional loading effects are involved. However, there are still limitations on the blind prediction of fracture properties along arbitrary loading directions.

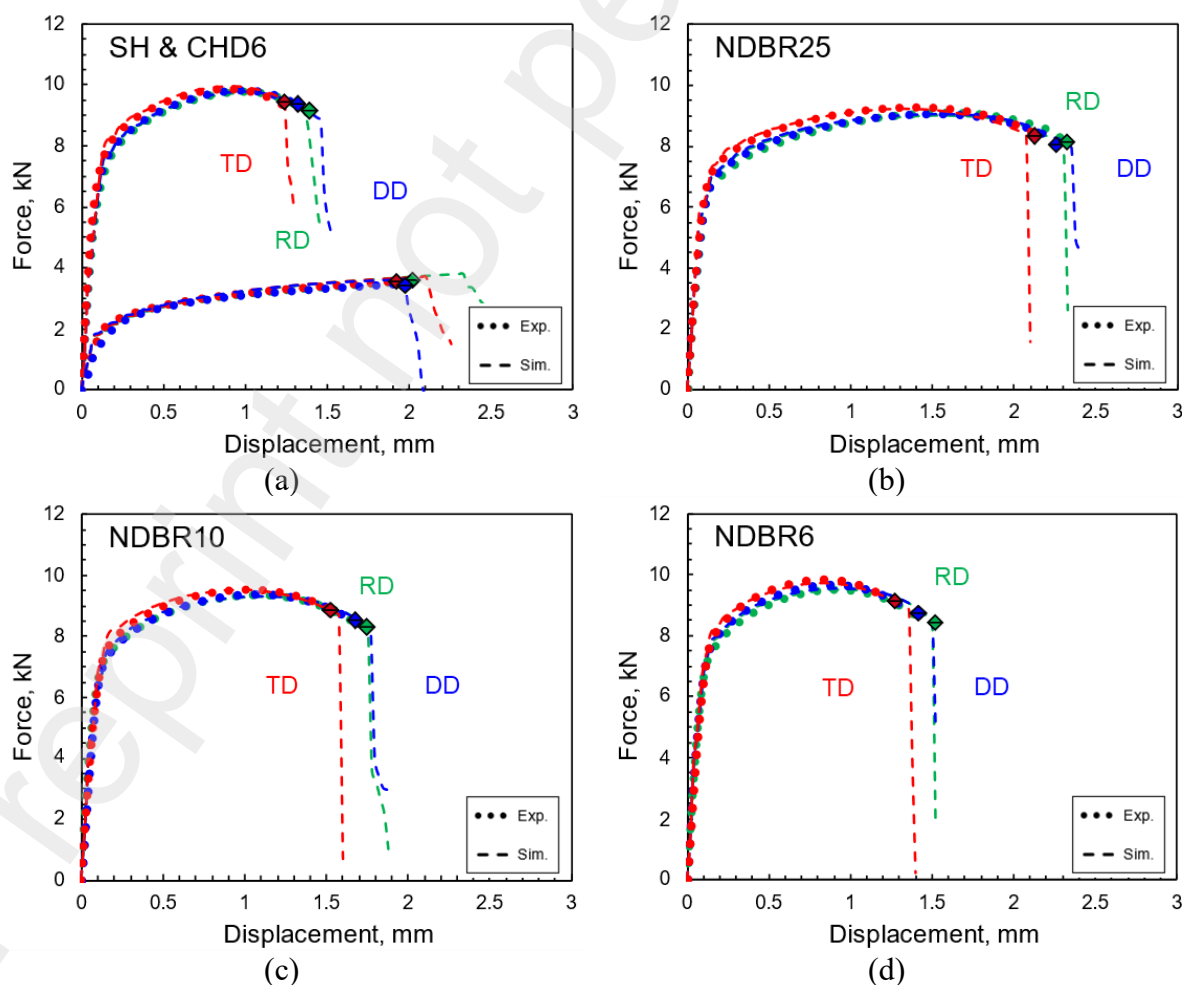


Figure 13: Prediction of fracture behavior of all tests using the fully anisotropic fracture model calibrated based on inputs of RD and TD (2D): (a) SH and CHD6, (b) NDBR25, (c) NDBR10, and (d) NDBR6.

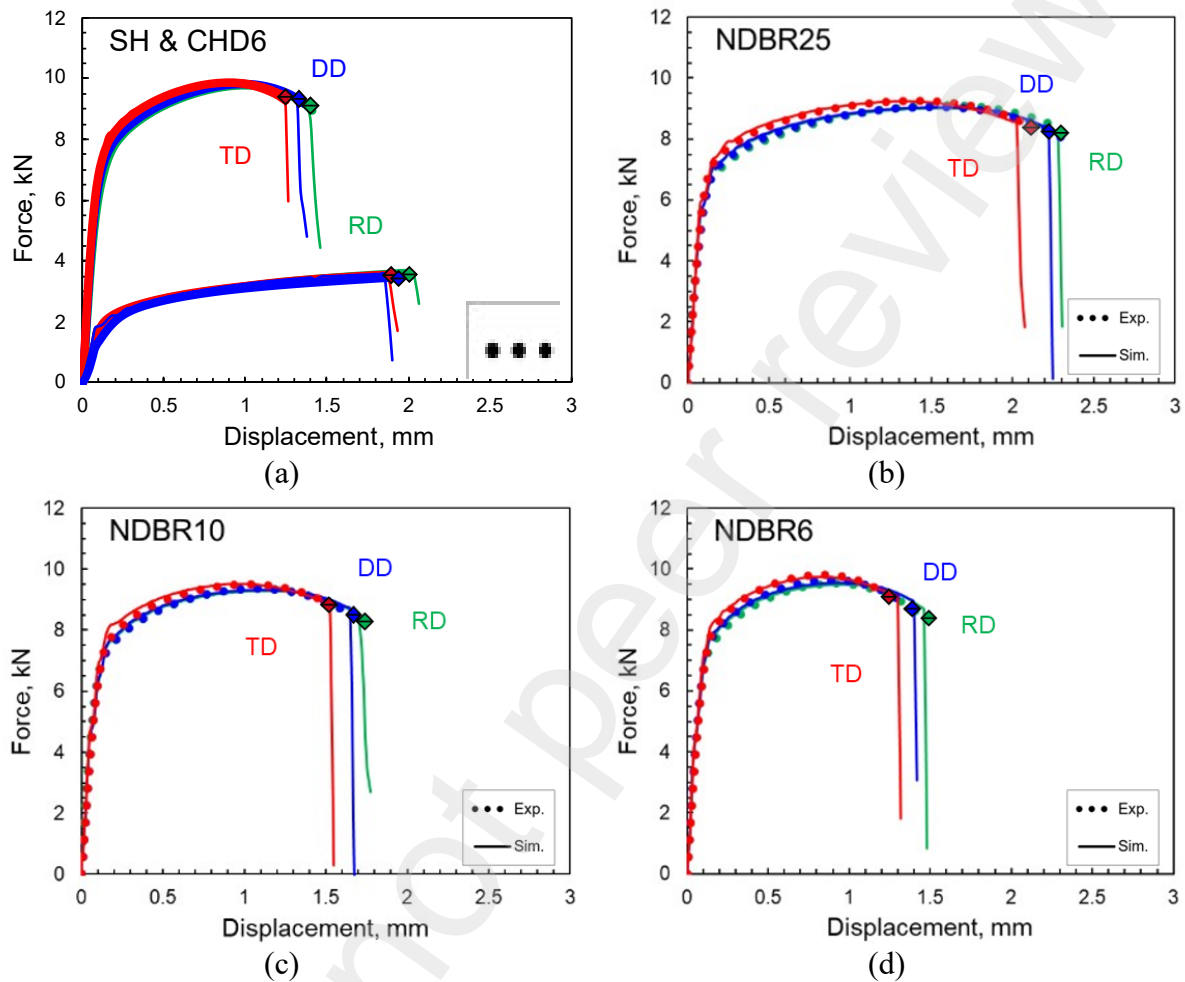
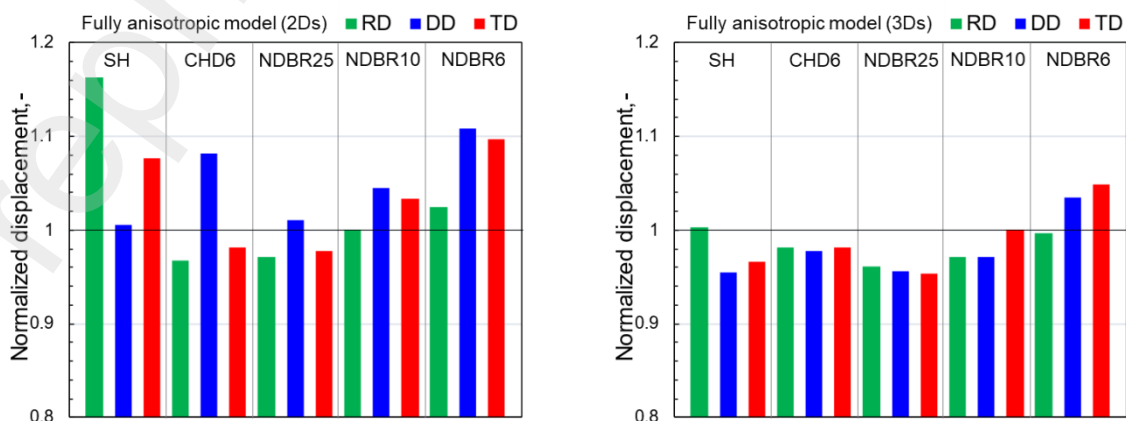


Figure 14: Prediction of fracture behavior of all tests using the fully anisotropic fracture model calibrated based on inputs of three loading directions (3D): (a) SH and CHD6, (b) NDBR25, (c) NDBR10, and (d) NDBR6.



(a)

(b)

Figure 15: Evaluation of the performance of the fully anisotropic fracture model on predicted normalized fracture displacements, parameters calibrated based on inputs of (a) RD and TD, and (b) three loading directions.

7 Discussion on the orientation dependency

The loading direction plays an important role in the accurate prediction of the ductile fracture in the investigated material. As shown in Figure 16, a comparison among all four types of models mentioned above is plotted. The deviation is calculated between the experimental fracture displacement and predicted value and then averaged among all five geometries for each direction. From the results, for partially anisotropic fracture models, either determined from RD or TD, accurate prediction can be achieved only at the corresponding direction with either 2% or 3%, while for other directions, the deviation could rise beyond 5%. For fully anisotropic fracture models, a large distinction exists between the one determined by only two directions and all three directions. The prediction of the fully anisotropic fracture model with two directional inputs on RD and TD has similar accuracy to the one from partially anisotropic fracture models; however, the prediction of fracture displacement gets more evenly distributed among three directions with a 5% deviation. On the other hand, the fully anisotropic fracture model with three directional inputs generates the best prediction in all directions. The deviation after averaging among three directions is below 3%.

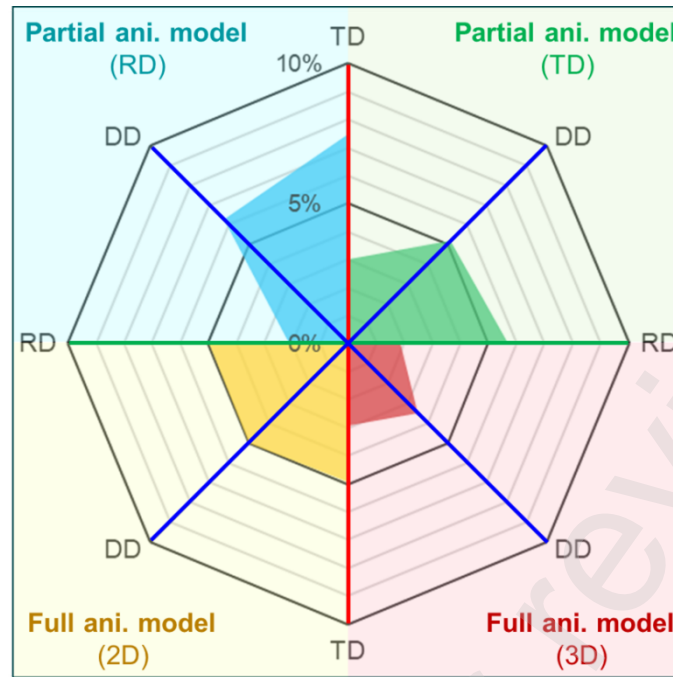


Figure 16: Comparison of the deviation of the partially and fully anisotropic models on predicted normalized fracture displacement.

8 Conclusions

The anisotropic effects on the deformation and fracture properties of QP1000 have been investigated experimentally and numerically under wide loading conditions. Based on the results presented in this study, several conclusions can be drawn.

- The investigated QP1000 steel demonstrates a good combination of strength and formability, with a high yield strength of over 750 MPa averaged among three loading directions and an excellent total elongation of at least 23.10%.
- The QP1000 steel shows minor to intermediate plastic anisotropy, which evolves clearly over the plastic deformation. However, pronounced anisotropic fracture behavior has been observed. For loading along the rolling direction (RD), diagonal direction (DD), and transverse direction (TD), the worst fracture resistance is along the TD, while the best varies between RD and DD loading.

- The anisotropic fracture behavior of QP1000 is highly dependent on the stress states. It is discovered from the current study that higher stress triaxiality intensifies the level of anisotropic fracture significantly in terms of both the fracture displacement and the failure strain.
- Partially anisotropic fracture models with anisotropic plasticity model but isotropic fracture model can only provide accurate fracture prediction for the loading direction that was used for the calibration of the fracture model but fails in other loading directions due to the pronounced and stress-state-dependent anisotropic fracture behavior of the material.
- A fully anisotropic hybrid damage mechanics model is formulated based on the linear transformation of plastic stains in the damage initiation criterion. A detailed calibration procedure is demonstrated considering testing data along two directions and three directions. It is shown that the latter case provides a satisfactory prediction of the anisotropic fracture across a large range of stress states.

Acknowledgments

The financial support by the Technology Industries of Finland Centennial Foundation via projects 691, 1492, and 2156 is gratefully acknowledged. The authors also wish to acknowledge the CSC – IT Center for Science, Finland, for computational resources under projects 2001353, 2004967, and 2009257. The Aalto internal seed funding for cooperation initiatives with the Technical University of Munich (TUM) is also acknowledged.

Author Statement

Zinan Li: Data curation, Formal analysis, Investigation, Software, Validation, Visualization, Writing - original draft.

Fuhui Shen: Methodology, Investigation, Supervision, Writing - review & editing.

Yi Liu: Data curation, Formal analysis.

Christoph Hartmann: Data curation, Formal analysis.

Roman Norz: Data curation, Formal analysis, Writing - review & editing.

Sebastian Münstermann: Supervision, Writing - review & editing.

Wolfram Volk: Supervision, Writing - review & editing.

Junying Min: Supervision, Writing - review & editing.

Junhe Lian: Conceptualization, Methodology, Writing - review & editing, Supervision, Project administration, Resources, Funding acquisition.

References

- [1] Bouaziz O, Zurob H, Huang M. Driving force and logic of development of advanced high strength steels for automotive applications. *Steel Res Int.* 2013;84:937-47.
- [2] Speer J, Matlock DK, De Cooman BC, Schroth J. Carbon partitioning into austenite after martensite transformation. *Acta Mater.* 2003;51:2611-22.
- [3] He J, Han G, Li S, Zou D. To correlate the phase transformation and mechanical behavior of QP steel sheets. *International Journal of Mechanical Sciences.* 2019;152:198-210.
- [4] Speer J, Matlock DK, De Cooman BC, Schroth JG. Carbon partitioning into austenite after martensite transformation. *Acta Mater.* 2003;51:2611-22.
- [5] De Moor E, Lacroix S, Clarke AJ, Penning J, Speer JG. Effect of Retained Austenite Stabilized via Quench and Partitioning on the Strain Hardening of Martensitic Steels. *Metallurgical and Materials Transactions A.* 2008;39:2586.
- [6] Seo EJ, Cho L, Estrin Y, De Cooman BC. Microstructure-mechanical properties relationships for quenching and partitioning (Q&P) processed steel. *Acta Mater.* 2016;113:124-39.
- [7] Ghosh S, Kaikkonen P, Javaheri V, Kaijalainen A, Miettunen I, Somani M, et al. Design of tough, ductile direct quenched and partitioned advanced high-strength steel with tailored silicon content. *Journal of Materials Research and Technology.* 2022;17:1390-407.
- [8] Mohtadi-Bonab MA, Ariza EA, Loureiro RCP, Centeno D, Carvalho FM, Avila JA, Masoumi M. Improvement of tensile properties by controlling the microstructure and crystallographic data in commercial pearlitic carbon-silicon steel via quenching and partitioning (Q&P) process. *Journal of Materials Research and Technology.* 2023;23:845-58.
- [9] Xu N, Wang L, Hu J, Xue W, Xu W. Enhancing the yield strength of intercritically annealed Q&P steel via bainite-based quenching and partitioning treatment. *Journal of Materials Research and Technology.* 2023;27:3996-4004.
- [10] Zhang Y, Wang J, Zhu N, Sun B, He Y, Xu X, et al. Investigation on strength and plasticity enhancement mechanism of 1180 MPa-grade quenching and partitioning steel. *Journal of Materials Research and Technology.* 2023;26:371-82.
- [11] Chen X, Niu C, Lian C, Lin J. The evaluation of formability of the 3rd generation advanced high strength steels QP980 based on digital image correlation method. *Procedia Engineer.* 2017;207:556-61.
- [12] Roth CC, Mohr D. Ductile fracture experiments with locally proportional loading histories. *International Journal of Plasticity.* 2016;79:328-54.
- [13] Mu L, Wang Y, Zang Y, Araujo Stemler PM. Edge Fracture Prediction Using Uncoupled

Ductile Fracture Models for DP780 Sheet. *Journal of Failure Analysis and Prevention*. 2017;17:321-9.

[14] Roth CC, Mohr D. Determining the strain to fracture for simple shear for a wide range of sheet metals. *International Journal of Mechanical Sciences*. 2018;149:224-40.

[15] Celada-Casero C, Vercruysse F, Linke B, Smith A, Kok P, Sietsma J, Santofimia MJ. Analysis of work hardening mechanisms in Quenching and Partitioning steels combining experiments with a 3D micro-mechanical model. *Materials Science and Engineering: A*. 2022;846:143301.

[16] Salehiyan D, Samei J, Amirkhiz BS, Hector LG, Wilkinson DS. Microstructural evolution during deformation of a QP980 steel. *Metallurgical and Materials Transactions A*. 2020;51:4524-39.

[17] Bai Y, Wierzbicki T. A new model of metal plasticity and fracture with pressure and Lode dependence. *International Journal of Plasticity*. 2008;24:1071-96.

[18] Sedlatschek T, Lian J, Li W, Jiang M, Wierzbicki T, Bazant MZ, Zhu J. Large-deformation plasticity and fracture behavior of pure lithium under various stress states. *Acta Mater*. 2021;208:116730.

[19] Mohr D, Marcadet SJ. Micromechanically-motivated phenomenological Hosford–Coulomb model for predicting ductile fracture initiation at low stress triaxialities. *Int J Solids Struct*. 2015;67-68:40-55.

[20] Dunand M, Mohr D. On the predictive capabilities of the shear modified Gurson and the modified Mohr–Coulomb fracture models over a wide range of stress triaxialities and Lode angles. *J Mech Phys Solids*. 2011;59:1374-94.

[21] Bai Y, Wierzbicki T. Application of extended Mohr–Coulomb criterion to ductile fracture. *Int J Fracture*. 2010;161:1-20.

[22] Xu S, Qian L, Sun C, Liu F, Wang C, Sun Z, Zhou Y. Investigation into the fracture behavior of ZK60 Mg alloy rolling sheet under different stress triaxiality. *Journal of Materials Research and Technology*. 2023;27:7368-79.

[23] Jia W, Wang L, Ma L, Li H, Xie H, Yuan Y. Deformation failure behavior and fracture model of twin-roll casting AZ31 alloy under multi-axial stress state. *Journal of Materials Research and Technology*. 2022;17:2047-58.

[24] Tekoglu C, Leblond JB, Pardoën T. A criterion for the onset of void coalescence under combined tension and shear. *J Mech Phys Solids*. 2012;60:1363-81.

[25] Gurson AL. Continuum theory of ductile rupture by void nucleation and growth: Part I—yield criteria and flow rules for porous ductile media. *J Eng Mater-T Asme*. 1977;99:2-15.

- [26] Nahshon K, Hutchinson JW. Modification of the Gurson Model for shear failure. *Eur J Mech a-Solid*. 2008;27:1-17.
- [27] Xue L. Constitutive modeling of void shearing effect in ductile fracture of porous materials. *Engineering Fracture Mechanics*. 2008;75:3343-66.
- [28] Nielsen KL, Tvergaard V. Effect of a shear modified Gurson model on damage development in a FSW tensile specimen. *Int J Solids Struct*. 2009;46:587-601.
- [29] Nielsen KL, Pardo T, Tvergaard V, de Meester B, Simar A. Modelling of plastic flow localisation and damage development in friction stir welded 6005A aluminium alloy using physics based strain hardening law. *Int J Solids Struct*. 2010;47:2359-70.
- [30] Malcher L, Pires FMA, de Sa JMAC. An assessment of isotropic constitutive models for ductile fracture under high and low stress triaxiality. *International Journal of Plasticity*. 2012;30-31:81-115.
- [31] Cao TS, Bobadilla C, Montmitonnet P, Bouchard PO. A comparative study of three ductile damage approaches for fracture prediction in cold forming processes. *J Mater Process Tech*. 2015;216:385-404.
- [32] Nonn A, Paredes M, Keim V, Wierzbicki T. Comparison of Fracture Models to Quantify the Effects of Material Plasticity on the Ductile Fracture Propagation in Pipelines. 2018:V003T05A5.
- [33] Wu H, Zhuang X, Zhang W, Zhao Z. Anisotropic ductile fracture: experiments, modeling, and numerical simulations. *Journal of Materials Research and Technology*. 2022;20:833-56.
- [34] Lian J, Sharaf M, Archie F, Münstermann S. A hybrid approach for modelling of plasticity and failure behaviour of advanced high-strength steel sheets. *International Journal of Damage Mechanics*. 2013;22:188-218.
- [35] Li Z, Chang Y, Liu W, Lian J. Predicting edge fracture in dual-phase steels: significance of anisotropy-induced localization Available at SSRN: <https://ssrn.com/abstract=4670747>. 2023.
- [36] Pineau A, Benzerga AA, Pardo T. Failure of metals I: Brittle and ductile fracture. *Acta Mater*. 2016;107:424-83.
- [37] Tekkaya AE, Bouchard PO, Bruschi S, Tasan CC. Damage in metal forming. *CIRP Annals*. 2020;69:600-23.
- [38] Wang S, Wang Y, Yu L, Ji K, Liu X, Lou Y. Failure Modeling for QP980 Steel by a Shear Ductile Fracture Criterion. *Metals-Basel*. 2022;12:452.
- [39] Brozzo P, Deluca B, Rendina R. A new method for the prediction of formability limits in metal sheets. *Proc 7th biennial Conf IDDR1972*.
- [40] Oh SI, Chen CC, Kobayashi S. Ductile Fracture in Axisymmetric Extrusion and

Drawing—Part 2: Workability in Extrusion and Drawing. *J Eng Ind.* 1979;101:36-44.

[41] Rice JR, Tracey DM. On ductile enlargement of voids in triaxial stress fields. *J Mech Phys Solids.* 1969;17:201-17.

[42] Lou Y, Huh H, Lim S, Pack K. New ductile fracture criterion for prediction of fracture forming limit diagrams of sheet metals. *Int J Solids Struct.* 2012;49:3605-15.

[43] Chen Z, Wang Y, Lou Y. User-friendly anisotropic hardening function with non-associated flow rule under the proportional loadings for BCC and FCC metals. *Mech Mater.* 2022;165:104190.

[44] Hou Y, Min J, Stoughton TB, Lin J, Carsley JE, Carlson BE. A non-quadratic pressure-sensitive constitutive model under non-associated flow rule with anisotropic hardening: Modeling and validation. *International Journal of Plasticity.* 2020;135:102808.

[45] Hou Y, Min J, Guo N, Shen Y, Lin J. Evolving asymmetric yield surfaces of quenching and partitioning steels: Characterization and modeling. *J Mater Process Tech.* 2021;290:116979.

[46] Jacques PJ, Furnémont Q, Lani F, Pardoen T, Delannay F. Multiscale mechanics of TRIP-assisted multiphase steels: I. Characterization and mechanical testing. *Acta Mater.* 2007;55:3681-93.

[47] Zhang C, Lou Y. Characterization and modelling of evolving plasticity behaviour up to fracture for FCC and BCC metals. *J Mater Process Tech.* 2023;317:117997.

[48] Hou Y, Lee M-G, Lin J, Min J. Experimental characterization and modeling of complex anisotropic hardening in quenching and partitioning (Q&P) steel subject to biaxial non-proportional loadings. *International Journal of Plasticity.* 2022;156:103347.

[49] Lian J, Shen F, Jia X, Ahn D-C, Chae D-C, Münstermann S, Bleck W. An evolving non-associated Hill48 plasticity model accounting for anisotropic hardening and r-value evolution and its application to forming limit prediction. *Int J Solids Struct.* 2018;151:20-44.

[50] Beese AM, Luo M, Li Y, Bai Y, Wierzbicki T. Partially coupled anisotropic fracture model for aluminum sheets. *Engineering Fracture Mechanics.* 2010;77:1128-52.

[51] Luo M, Dunand M, Mohr D. Experiments and modeling of anisotropic aluminum extrusions under multi-axial loading – Part II: Ductile fracture. *International Journal of Plasticity.* 2012;32-33:36-58.

[52] Ha J, Baral M, Korkolis YP. Plastic anisotropy and ductile fracture of bake-hardened AA6013 aluminum sheet. *Int J Solids Struct.* 2018;155:123-39.

[53] Paredes M, Lian J, Wierzbicki T, Cristea ME, Münstermann S, Darcis P. Modeling of plasticity and fracture behavior of X65 steels: seam weld and seamless pipes. *Int J Fracture.* 2018;213:17-36.

- [54] Jia Y, Bai Y. Ductile fracture prediction for metal sheets using all-strain-based anisotropic eMMC model. *International Journal of Mechanical Sciences*. 2016;115-116:516-31.
- [55] Khan AS, Liu H. Strain rate and temperature dependent fracture criteria for isotropic and anisotropic metals. *International Journal of Plasticity*. 2012;37:1-15.
- [56] Shen F, Münstermann S, Lian J. Investigation on the ductile fracture of high-strength pipeline steels using a partial anisotropic damage mechanics model. *Engineering Fracture Mechanics*. 2020;227:106900.
- [57] Lian J, Liu P, Münstermann S. Modeling of damage and failure of dual phase steel in Nakajima test. *Key Engineering Materials*. 2012;525-526:69-72.
- [58] Lian J, Wierzbicki T, Zhu J, Li W. Prediction of shear crack formation of lithium-ion batteries under rod indentation: Comparison of seven failure criteria. *Engineering Fracture Mechanics*. 2019;217:106520.
- [59] Liu W, Lian J, Münstermann S, Zeng C, Fang X. Prediction of crack formation in the progressive folding of square tubes during dynamic axial crushing. *International Journal of Mechanical Sciences*. 2020;176:105534.
- [60] Shen F, Münstermann S, Lian J. Forming limit prediction by the Marciniak–Kuczynski model coupled with the evolving non-associated Hill48 plasticity model. *J Mater Process Tech*. 2021;287:116384.
- [61] Aretz H. Numerical analysis of diffuse and localized necking in orthotropic sheet metals. *International Journal of Plasticity*. 2007;23:798-840.
- [62] Bao Y, Wierzbicki T. On the cut-off value of negative triaxiality for fracture. *Engineering Fracture Mechanics*. 2005;72:1049-69.
- [63] Barlat F, Brem JC, Yoon JW, Chung K, Dick RE, Lege DJ, et al. Plane stress yield function for aluminum alloy sheets—part 1: theory. *International Journal of Plasticity*. 2003;19:1297-319.
- [64] Barlat F, Aretz H, Yoon JW, Karabin ME, Brem JC, Dick RE. Linear transformation-based anisotropic yield functions. *International Journal of Plasticity*. 2005;21:1009-39.
- [65] Aretz H, Barlat F. New convex yield functions for orthotropic metal plasticity. *International Journal of Non-Linear Mechanics*. 2013;51:97-111.
- [66] Lou Y, Yoon JW. Anisotropic ductile fracture criterion based on linear transformation. *International Journal of Plasticity*. 2017;93:3-25.
- [67] Park N, Stoughton TB, Yoon JW. A new approach for fracture prediction considering general anisotropy of metal sheets. *International Journal of Plasticity*. 2020;124:199-225.
- [68] Park N, Huh H, Yoon JW. Anisotropic fracture forming limit diagram considering non-

directionality of the equi-biaxial fracture strain. Int J Solids Struct. 2018;151:181-94.

[69] Lou Y, Yoon JW. A user-friendly anisotropic ductile fracture criterion for sheet metal under proportional loading. Int J Solids Struct. 2021;217-218:48-59.